

Dynamic Modeling and Simulation of an Autonomous
Underwater Vehicle (AUV)

A Thesis

SUBMITTED TO THE FACULTY OF THE
UNIVERSITY OF MINNESOTA

BY

Kevin Orpen

IN PARTIAL FULFILLMENT OF THE REQUIREMENTS

FOR THE DEGREE OF

Bachelor of Aerospace Engineering and Mechanics

With Honors

Faculty Adviser: Professor Junaed Sattar, PhD

May 2021

Copyright Page

Copyright © 2021 by Kevin Orpen

Acknowledgements

This thesis, and my overall experience with the world of underwater robotics, would not have been possible without my adviser, Professor Junaed Sattar. I want to thank you for welcoming me into the Interactive Robotics and Vision Laboratory with open arms. You have always been such a strong advocate of mine and supported my learning throughout these past years, and for that, I will forever be grateful.

I would also like to thank Professors Maziar Hemati and Yohannes Ketema for serving on my thesis committee. Your support and dedication to my research has greatly helped me refine my work and make this final product a reality.

Abstract

Autonomous Underwater Vehicles (AUVs) have been in development in recent decades to address the difficulties and high costs of oceanic exploration, with applications including marine life monitoring, search and rescue operations, and wreck inspection. An underwater robot developed by the Interactive Robotics and Vision (IRV) Laboratory at the University of Minnesota is LoCO, a Low Cost Open-Source AUV. LoCO seeks to assist in a number of underwater applications while reducing the current high cost of entry into underwater robotics. One aspect of this underwater vehicle that is integral to its capacity as an AUV is the modeling of its dynamics, and each new AUV comes with unique geometries spanning various propulsion control methods for specializing in different underwater tasks. This thesis seeks to establish an underwater dynamic model for the robot, implement the model in a simulated setting so as to provide testing opportunities before field deployment, and compare the effectivity of the model to collected experimental data. This, in turn, will lead to the efficient development of its autonomous systems and capability to assist in underwater operations. Within this research, the dynamic models have been produced and geometry-dependent coefficients have been derived for LoCO. A simulator for the robot has also been developed that can interface with onboard software. Though the simulation agrees relatively well with experimental data collected for LoCO's forward motion, there are still other motion modes that require further investigation. Overall, this dynamic foundation will provide for future control system and other autonomous development to further its underwater capabilities.

Table of Contents

List of Tables	vi
List of Figures	vii
Chapter 1 Introduction.....	1
1.1. Background	1
1.2. LoCO Design.....	2
1.3. Thesis Objective.....	3
1.4. Overview	4
Chapter 2 Derivation of Dynamic Equations	5
2.1. Introduction	5
2.2. Body Frame Definition.....	5
2.3. Relationship Between Inertial and Body Coordinate Frames	8
2.4. Rigid Body 6-Degrees of Freedom Equations of Motion	10
2.5. Forces and Moments	12
2.5.1. Environmental Forces	12
2.5.2. Propulsion	13
2.5.3. Restoring Forces	14
2.5.4. Added Mass	14

2.5.5.	Hydrodynamic Damping.....	17
2.6.	Overall Kinetics Equations.....	19
2.7.	Conclusion.....	20
Chapter 3	Estimation of LoCO Dynamic Parameters	21
3.1.	Introduction	21
3.2.	Buoyancy.....	21
3.3.	Mass and Moments of Inertia.....	23
3.4.	Added Mass Coefficients	26
3.5.	Hydrodynamic Damping Coefficients	36
3.6.	Dynamic Equations for LoCO.....	42
3.7.	Conclusion.....	44
Chapter 4	Simulation.....	46
4.1.	Introduction	46
4.2.	Modeling and Visualization	46
4.3.	Physics.....	48
4.4.	Simulation Architecture and Control	49
4.5.	Quaternions and Force Application.....	50
4.6.	Conclusion.....	51
Chapter 5	Experimental Data and Comparison with Simulation	53

5.1. Introduction	53
5.2. Experiment and Data Analysis	53
5.3. Simulation Data Comparison	55
5.4. Conclusion.....	57
Chapter 6 Conclusion	58
6.1. Review.....	58
6.2. Conclusions	58
6.3. Future Work	59
References.....	60
Appendix A.....	63

List of Tables

Table 1: Vehicle buoyancy analysis summary.....	22
Table 2: Vehicle mass and moments of inertia analysis summary.	25
Table 3: Table of components and corresponding variable names for geometric LoCO models.	29
Table 4: Added mass analysis values.....	36
Table 5: Summary of component coefficients of drag.....	38
Table 6: Summary of component drag reference areas.	38
Table 7: Summary of hydrodynamic damping analysis results.	42
Table 8: Relevant dynamic model parameters from analysis and estimation.....	43
Table 9: LoCO Component Matrix for mass and moment of inertia determination.	64

List of Figures

Figure 1: LoCO in untethered deployment in the Caribbean Sea near Barbados [4].	2
Figure 2: LoCO CAD model in SolidWorks.	2
Figure 3: LoCO body-fixed coordinate frame definition overall view.	6
Figure 4: LoCO body-fixed coordinate frame definition section views.	7
Figure 5: Relationship between body frame and inertial frame.	8
Figure 6: Example of notation for rectangular prism of square cross section rotating about one end (rotation about the dashed line).	18
Figure 7: Moments of inertia for hollow cylinder and rectangular prism [20].	24
Figure 8: Parallel axis theorem example, where m is mass of the object.	25
Figure 9: Geometric approximation for LoCO flow in x-direction – “X-Model”.	28
Figure 10: Geometric approximation for LoCO flow in y-direction – “Y-Model”.	28
Figure 11: Geometric approximation for LoCO flow in z-direction – “Z-Model”.	29
Figure 12: Added mass parameters for a circle and a square [13], [21].	30
Figure 13: LoCO in a simulated Gazebo world.	47
Figure 14: ROS program nodes and messages used to run the simulation.	50
Figure 15: Thruster force versus PWM input [28].	54
Figure 16: Velocity versus forward thrust applied for a straight line, horizontal path in a pool.	55
Figure 17: Velocity versus full forward thrust applied for a straight line, horizontal path.	56

Figure 18: Clockwise penetrator numbering convention..... 64

Chapter 1

Introduction

1.1. Background

Ocean exploration began in the late 19th century with the search for a greater understanding of how the Earth works and the life it holds. Since then, discoveries across the span of 71% of the Earth's surface have yielded entirely new fields of study and revolutionary findings in areas such as geology, marine biology, and environmental science. However, the majority of Earth's oceans remain unexplored, due in part to high resource and economic costs [1]. This, along with the quest to explore deep sea areas extremely difficult for humans to reach, has spurred the field of underwater robotics. Autonomous Underwater Vehicles (AUVs) have been in development in recent decades to address the high cost of underwater exploration. Other applications of these technologies include marine life monitoring, mineral exploration, global environment evaluation, wreck inspection, and search and rescue operations. The dynamic underwater environment comes with a host of new challenges though, ranging from navigation where GPS does not function to environments of operation prone to unpredictable disturbances [2]. An example of underwater robotics development for oceanography research can be found with the Seaglider [3], where the AUV is designed to operate for long periods of time to gather ocean data at a fraction of the cost of manned expeditions. Though research in underwater robotics has greatly progressed, the sensors and equipment required for accurate navigation and reliable operation in underwater environments often come at high costs.

1.2. LoCO Design

An AUV developed by the Interactive Robotics and Vision (IRV) Laboratory at the University of Minnesota is LoCO. LoCO AUV is a Low-Cost, Open-Source, Autonomous Underwater Vehicle. It is vision-guided and rated to a depth of 100 meters, capable of being deployed by a single person in the field [4]. A picture of LoCO in an ocean deployment can be seen below, along with the corresponding Computer Aided Design (CAD) model in SolidWorks. This underwater vehicle seeks to assist personnel in numerous underwater applications in a more cost-effective manner than previous robots.



Figure 1: LoCO in untethered deployment in the Caribbean Sea near Barbados [4].

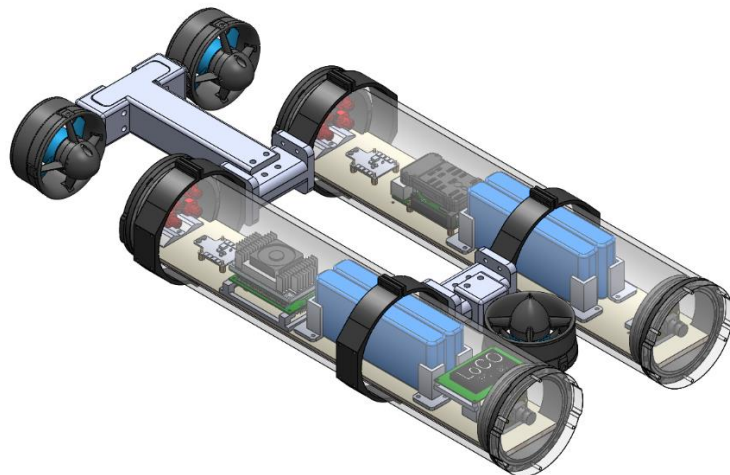


Figure 2: LoCO CAD model in SolidWorks.

One aspect of LoCO that is integral to its capacity as an AUV is the modeling of its dynamics. For a reliable control system to be developed that enables autonomous operation, a foundation in the dynamics of the robot must be established. Though a number of studies have been conducted on the modeling of AUVs in an underwater environment [5], [6], and the governing equations for marine hydrodynamics have been established, each new AUV comes with unique geometries. Further, AUV designs boast various propulsion control methods for the underwater tasks they are primarily designed for.

1.3. Thesis Objective

This thesis seeks to evaluate the known properties common to any underwater environment and apply foundational components to characterize the underwater dynamics of the LoCO AUV. Work is performed to implement these dynamics in a simulated environment, able to be integrated with onboard robot systems, in order to provide a mode of testing software before resource-costly field trials. Experimental testing data is compared to the simulation implementation of the dynamic model. These outcomes, in turn, will lead to the efficient development of future control systems to assist in underwater research including trash detection development, vision system development, and human-robot interaction research [7].

1.4. Overview

The content discussed herein serves to first provide a foundation in the governing dynamics and various definitions for LoCO in Chapter 2. A number of assumptions are previewed before a brief description of the relation between dynamics derived in the frame of a rigid body and the corresponding motion in an inertial frame. The general dynamic equations for a 6-Degrees-of-Freedom (DoF) body are derived and associated forces for the underwater robot are discussed. Chapter 3 takes these general equations and describes the various estimation methods used to evaluate the coefficient parameters in the dynamic equations specific to the vehicle. A final list of estimated parameters is presented along with the resulting simplified dynamic equations. Chapter 4 discusses the simulation component of the thesis, including its program architecture and application of forces. Chapter 5 looks at how the simulation is utilized to compare the dynamic model to experimental data collected. Finally, Chapter 6 summarizes the thesis in conclusion of the work.

Chapter 2

Derivation of Dynamic Equations

2.1. Introduction

Before any specific dynamic estimates regarding LoCO can be made, the dynamic framework and general equations of motion must be derived. Though these derivations can be found in a number of texts [8]–[10], they are included within this thesis so that the document may be self-sufficient. Governing assumptions that are being made for this dynamic model will be explained in each of the appropriate sections, but are listed below as an overview [8]:

- 1) The AUV can be treated as a rigid body of a constant mass.
- 2) The earth's rotation is negligible for acceleration components of the vehicle's center of mass.
- 3) The thrusters are assumed to be a constant source of thrust.
- 4) The underwater vehicle is sufficiently submerged in an unbounded and ideal fluid.
- 5) The AUV does not experience underwater currents.
- 6) The AUV is assumed to not be a streamlined body due to external irregularities such as clamps.

2.2. Body Frame Definition

There are often two frames of reference used in expressing the equations of motion for an underwater vehicle. One of these is a “body” coordinate frame, which is fixed to the body of the marine vehicle. It is beneficial in many other applications to

attach the origin of the coordinate system to the center of gravity of the vehicle.

However, especially with a vehicle that can be modified such as LoCO, the center of gravity may change throughout the design cycle of the vehicle. Along with modeling benefits explained later regarding body-fixed origin placement along lines of symmetry, it is common to define the body-fixed coordinate frame origin at a location other than the center of gravity. The coordinate system for LoCO can be seen below in Fig. 3. In marine engineering, velocities in the x , y , and z directions are defined as surge (u), sway (v), and heave (w), respectively, with overall forces along the axes noted as X , Y , and Z .

Similarly, angular velocities about those same axes are defined as roll (p), pitch (q), and yaw (r), respectively, with overall moments along the axes noted as K , M , and N .

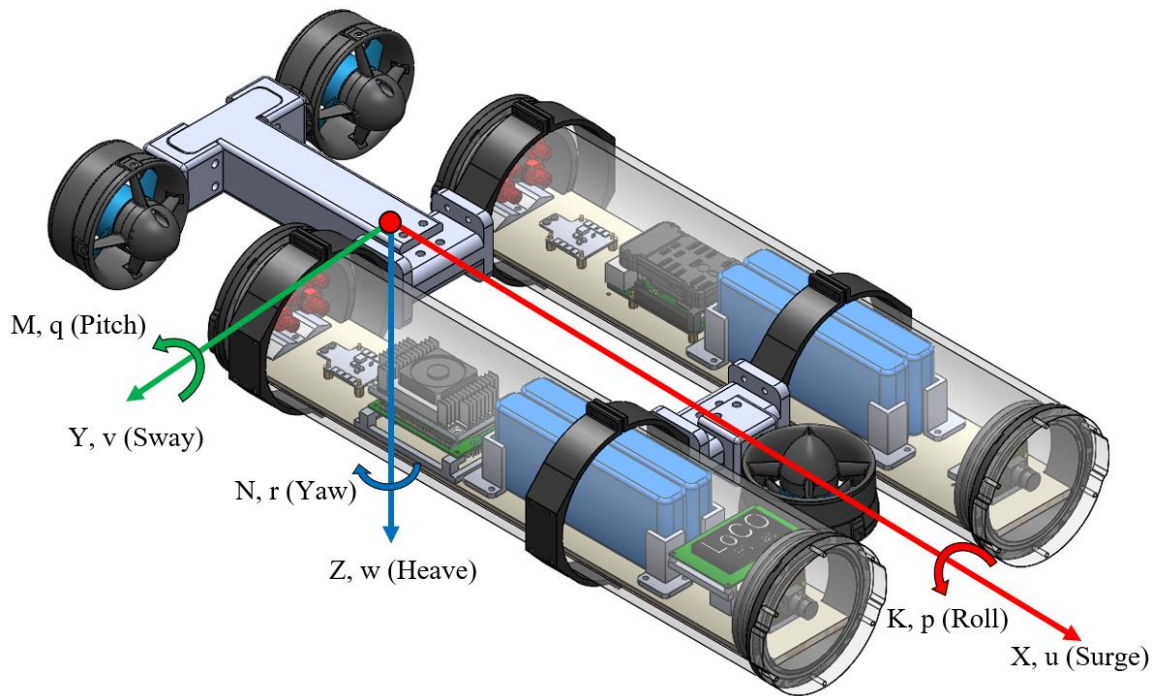


Figure 3: LoCO body-fixed coordinate frame definition overall view.

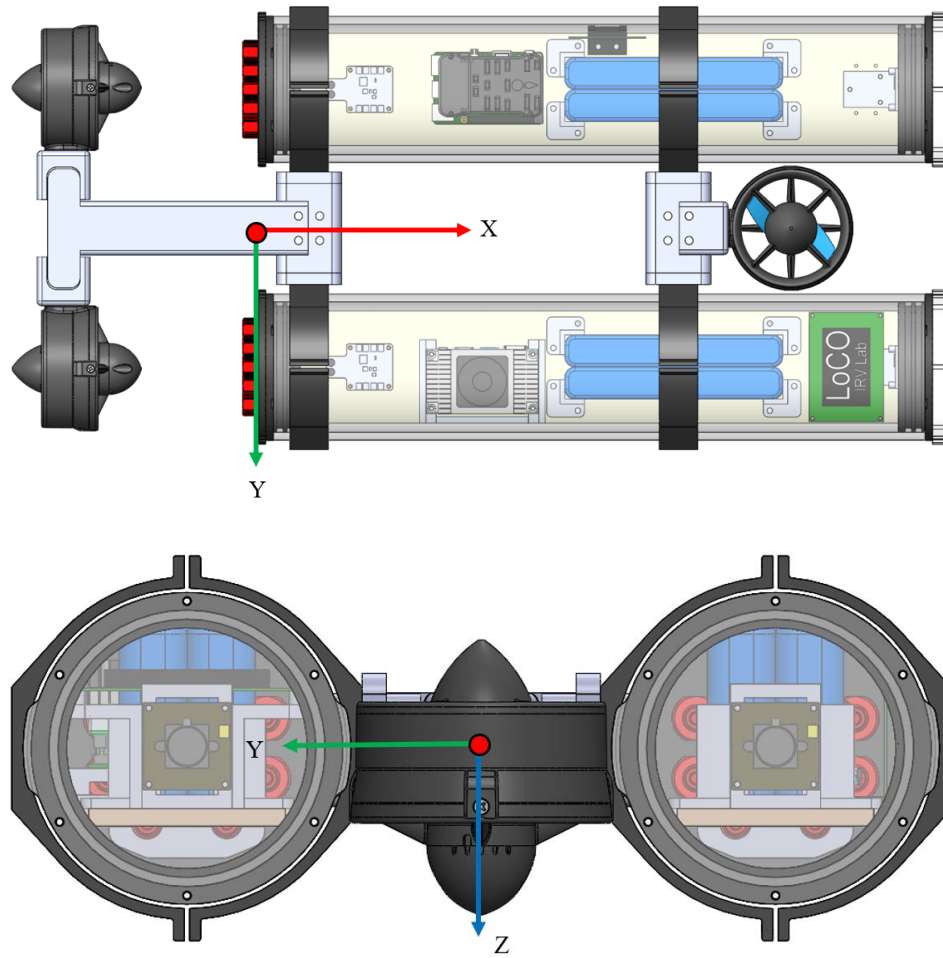


Figure 4: LoCO body-fixed coordinate frame definition section views.

As can be seen in Figs. 3 and 4, LoCO has geometric planes of symmetry about the x-z plane and x-y plane. For the case of this analysis, the body frame origin for LoCO is located at the intersection of these two planes and along the x axis to the back face of the rear end cap. This way, the characteristics of the robot can change with minimal effect to the dynamic framework of the thesis. More will be discussed on the force-related advantages to this origin location as well.

2.3. Relationship Between Inertial and Body Coordinate Frames

The second frame used as reference for these equations of motion is an inertial frame that the underwater vehicle operates in. For this analysis, an Earth-fixed inertial system will be used called “NED”, or “North-East-Down” [10]. In this case, the x direction of the coordinate system points North, the y direction points East, and the z direction therefore points downwards.

Though much of this thesis is devoted to the analysis of motion and forces in the body-fixed frame defined above, for any mission with an underwater vehicle, it is critical to relate the state of the vehicle back to the overall frame of reference. A visual depiction of the relation between the Earth-fixed frame and the body-fixed frame is given below in Fig. 5. The position of the vehicle in relation to the Earth frame is often given in terms of X_E , Y_E , and Z_E , along their respective axes. The angle of rotation about each of these axes is denoted as ϕ , θ , and ψ , respectively.

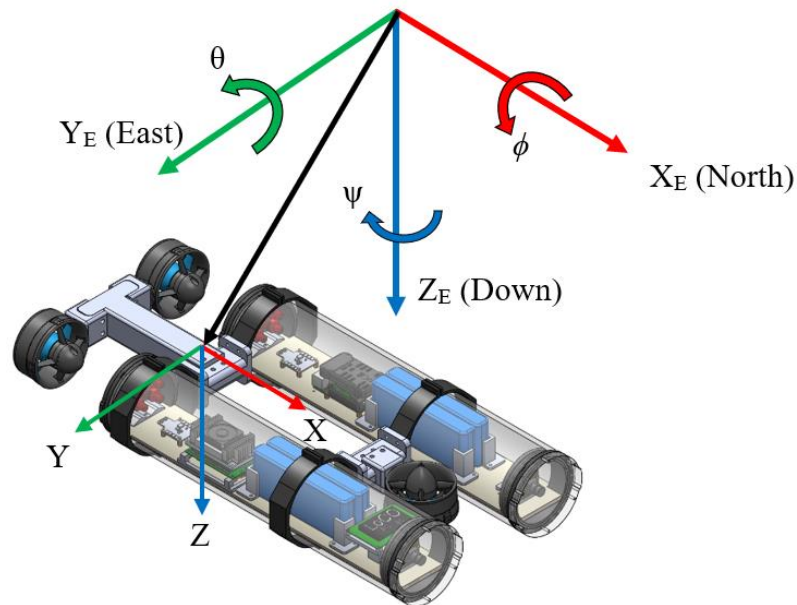


Figure 5: Relationship between body frame and inertial frame.

Euler angles give a way of relating the orientation of a rigid body in three-dimensional space with reference to an original reference frame through three single-axis rotations. Though there are multiple possible conventions for achieving this, one example is the Euler “3-2-1”, or “Z-Y-X”, sequence. Each rotation is represented by a 3 x 3 matrix, with the first rotation about the original z-axis by the yaw angle, denoted as $R_z(\psi)$. Then, a rotation about the following y-axis by the pitch angle is performed, and finally a rotation about the following x-axis by the roll angle. More detail on these rotation matrices and Euler angles can be found in various sources such as [11], [12]. Overall, a final relationship between the velocity of the underwater vehicle in Earth frame coordinates and body frame coordinates can then be represented as

$$\begin{aligned}
 \begin{bmatrix} u \\ v \\ w \end{bmatrix} &= R_x(\phi)R_y(\theta)R_z(\psi) \begin{bmatrix} \dot{X}_E \\ \dot{Y}_E \\ \dot{Z}_E \end{bmatrix} \\
 &= \begin{bmatrix} 1 & 0 & 0 \\ 0 & \cos(\phi) & \sin(\phi) \\ 0 & -\sin(\phi) & \cos(\phi) \end{bmatrix} \begin{bmatrix} \cos(\theta) & 0 & -\sin(\theta) \\ 0 & 1 & 0 \\ \sin(\theta) & 0 & \cos(\theta) \end{bmatrix} \begin{bmatrix} \cos(\psi) & \sin(\psi) & 0 \\ -\sin(\psi) & \cos(\psi) & 0 \\ 0 & 0 & 1 \end{bmatrix} \begin{bmatrix} \dot{X}_E \\ \dot{Y}_E \\ \dot{Z}_E \end{bmatrix} \\
 &= \begin{bmatrix} \cos(\theta)\cos(\psi) \\ -\sin(\psi)\cos(\phi) + \sin(\phi)\sin(\theta)\cos(\psi) \dots \\ \sin(\phi)\sin(\psi) + \cos(\phi)\cos(\psi)\sin(\theta) \\ \cos(\theta)\sin(\psi) \\ \cos(\phi)\cos(\psi) + \sin(\phi)\sin(\theta)\sin(\psi) \dots \\ -\sin(\phi)\cos(\psi) + \cos(\phi)\sin(\theta)\sin(\psi) \\ -\sin(\theta) \\ \sin(\phi)\cos(\theta) \\ \cos(\phi)\cos(\theta) \end{bmatrix} \begin{bmatrix} \dot{X}_E \\ \dot{Y}_E \\ \dot{Z}_E \end{bmatrix} \tag{1}
 \end{aligned}$$

To achieve a similar transformation for angular velocities, each Euler angle derivative must be addressed separately since they are not independent orthogonal elements. So,

$$\begin{bmatrix} p \\ q \\ r \end{bmatrix} = R_x(\phi)R_y(\theta)R_z(\psi) \begin{bmatrix} 0 \\ 0 \\ \dot{\psi} \end{bmatrix} + R_x(\phi)R_y(\theta) \begin{bmatrix} 0 \\ \dot{\theta} \\ 0 \end{bmatrix} + R_x(\phi) \begin{bmatrix} \dot{\phi} \\ 0 \\ 0 \end{bmatrix}$$

$$p = \dot{\phi} - \sin(\theta)\dot{\psi} \quad (2a)$$

$$q = \sin(\phi)\cos(\theta)\dot{\psi} + \cos(\phi)\dot{\theta} \quad (2b)$$

$$r = \cos(\phi)\cos(\theta)\dot{\psi} - \sin(\phi)\dot{\theta} \quad (2c)$$

One drawback of Euler angle representation of the motion of the vehicle is what is known as “gimbal lock”, or when there is a singularity in the equations of motion, such as that caused by a pitch value of 90 degrees. For the sake of expressing the relationships as most commonly used in marine dynamics, the resulting equations of motion as derived above hold their value since large pitch angles are usually avoided with submarines or other streamlined underwater vehicles [9]. An alternate way to express rotations are quaternions. Though they can be more complicated than expressions with Euler angles, they eliminate the issue with singularity and provide computationally easier ways to work with rotations. Quaternions, and how they are implemented in simulation, are discussed later.

2.4. Rigid Body 6-Degrees of Freedom Equations of Motion

As given in the first two assumptions, the equations of motion for LoCO can be derived as those for a rigid body with constant mass and six degrees of freedom. The

following set of equations applies to a body-fixed coordinate frame in which the center of gravity is not necessarily the center of the coordinate system, derived within Newton-Euler framework. This can be seen defined in Figs. 3 and 4 for LoCO, where the forces and moments of the following derivation are taken about the origin of the body system.

Beginning with an expression of Newton's second law, the forces on the body are equivalent to the time derivative of linear momentum. When dealing with rotating coordinate frames inside an overall inertial frame, rotational effects on changes in momentum must be compensated for besides linear acceleration. This leads to

$$\mathbf{F} = \frac{d}{dt}(m\mathbf{U}) = m \left(\dot{\mathbf{U}} + \boldsymbol{\omega} \times \mathbf{U} + \boldsymbol{\alpha} \times \mathbf{r}_G + \boldsymbol{\omega} \times (\boldsymbol{\omega} \times \mathbf{r}_G) \right) \quad (3)$$

where bold notation indicates vectors, in which \mathbf{U} is linear velocity of the vehicle origin, $\boldsymbol{\omega}$ is the angular velocity of the body system, $\boldsymbol{\alpha}$ is the angular acceleration, and \mathbf{r}_G is the position vector from the origin of the coordinate frame to the vehicle center of gravity. In this equation, the first term in the translational acceleration, the second is the Coriolis term, the third is the azimuthal acceleration, and the final term is the centripetal acceleration.

Now for the moments on the vehicle, the sum of these is equivalent to the time derivative of angular momentum. Similar to dealing with a rotating frame in equation 3,

$$\mathbf{M} = \frac{d}{dt}(\mathbf{I}\boldsymbol{\omega}) = \mathbf{I} \cdot \boldsymbol{\alpha} + \boldsymbol{\omega} \times (\mathbf{I} \cdot \boldsymbol{\omega}) + m \cdot \mathbf{r}_G \times (\dot{\mathbf{U}} + \boldsymbol{\omega} \times \mathbf{U}) \quad (4)$$

where the same notation is used from equation 3, and \mathbf{I} is the moment of inertia matrix for the body given with the matrix,

$$\mathbf{I} = \begin{bmatrix} I_x & -I_{xy} & -I_{xz} \\ -I_{yx} & I_y & -I_{yz} \\ -I_{zx} & -I_{zy} & I_z \end{bmatrix} \quad (5)$$

More in-depth derivations of these equations of motion can be found in sources such as [8]–[10]. Evaluating equation 3 for the axial force, lateral force, and vertical force equations,

$$X = m(\dot{u} - vr + wq - x_G(q^2 + r^2) + y_G(pq - \dot{r}) + z_G(pr - \dot{q})) \quad (6a)$$

$$Y = m(\dot{v} - wp + ur + x_G(qp + \dot{r}) - y_G(r^2 + p^2) + z_G(qr - \dot{p})) \quad (6b)$$

$$Z = m(\dot{w} - uq + vp + x_G(rp - \dot{q}) + y_G(rq + \dot{p}) - z_G(p^2 + q^2)) \quad (6c)$$

Evaluating equation 4 for the moment about the roll moment, pitch moment, and yaw moment,

$$\begin{aligned} K = I_x \dot{p} + (I_z - I_y)qr - (\dot{r} + pq)I_{xz} + (r^2 - q^2)I_{yz} + (pr - \dot{q})I_{xy} \dots \\ + m(y_G(\dot{w} - uq + vp) - z_G(\dot{v} - wp + ur)) \end{aligned} \quad (6d)$$

$$\begin{aligned} M = I_y \dot{q} + (I_x - I_z)rp - (\dot{p} + qr)I_{xy} + (p^2 - r^2)I_{xz} + (qp - \dot{r})I_{yz} \dots \\ + m(z_G(\dot{u} - vr + wq) - x_G(\dot{w} - uq + vp)) \end{aligned} \quad (6e)$$

$$\begin{aligned} N = I_z \dot{r} + (I_y - I_x)pq - (\dot{q} + rp)I_{yz} + (q^2 - p^2)I_{xy} + (rq - \dot{p})I_{xz} \dots \\ + m(x_G(\dot{v} - wp + ur) - y_G(\dot{u} - vr + wq)) \end{aligned} \quad (6f)$$

2.5. Forces and Moments

2.5.1. Environmental Forces

One of the primary assumptions for this dynamic analysis lies with the environmental forces. In a full seakeeping analysis of an underwater vehicle, surface effects, radiation-induced damping, and other wave effects are taken into account. These variables can come to be very dependent upon the situation involved for the vehicle.

Since LoCO is designed to operate in a range of environments, these wave-dependent

effects and surface effects are ignored with the assumption that the AUV is sufficiently submerged underwater.

2.5.2. Propulsion

The propulsion for LoCO is governed with three thrusters. The rear port and starboard thrusters control movement in the horizontal plane, while the vertical thruster adds control in the vertical plane. Each thruster is referred to as “port”, “stbd”, and “fore”, respectively. One assumption regarding the analysis with the thrusters is that they act as point forces at the center of the thruster propellers. Though the actual thrusters have inherent propeller dynamics, the point force simplification has been made for this analysis as a reasonable approximation. As for the reaction torques of each thruster, the port and starboard thrusters have propellers that provide the same forward thrust while spinning in opposite directions, so the moments cancel each other. It also assumed that the moment produced by the force thruster is negligible with respect to the larger vehicle dynamics and is ignored. With this, the forces and moments created by the thrusters can be expressed with the same conventions as established in section 2.4.

$$X_P = T_{port} + T_{stbd} \quad (7a)$$

$$Y_P = 0 \quad (7b)$$

$$Z_P = T_{fore} \quad (7c)$$

$$K_P = 0 \quad (7d)$$

$$M_P = -T_{fore} x_{fore} \quad (7e)$$

$$N_P = -T_{port} y_{port} - T_{stbd} y_{stbd} \quad (7f)$$

2.5.3. Restoring Forces

The gravity and buoyancy forces acting on an underwater vehicle are known as the restoring forces. To create a stable underwater vehicle, it is generally desired that the center of buoyancy and center of gravity are located at the same x and y positions with respect to the origin, and with the center of gravity lying below the center of buoyancy. This way, rotation of the vehicle from its resting state causes a corrective “restoring” moment to be applied to the vehicle. As derived in more detail in [10], these resulting forces and moments can be expressed as

$$X_R = -(W - B)\sin(\theta) \quad (8a)$$

$$Y_R = (W - B)\cos(\theta)\sin(\phi) \quad (8b)$$

$$Z_R = (W - B)\cos(\theta)\cos(\phi) \quad (8c)$$

$$K_R = (y_G W - y_B B)\cos(\theta)\cos(\phi) - (z_G W - z_B B)\cos(\theta)\sin(\phi) \quad (8d)$$

$$M_R = -(x_G W - x_B B)\cos(\theta)\cos(\phi) - (z_G W - z_B B)\sin(\theta) \quad (8e)$$

$$N_R = (x_G W - x_B B)\cos(\theta)\sin(\phi) - (y_G W - y_B B)\sin(\theta) \quad (8f)$$

where W represents the dry weight of the AUV, and B is the buoyancy force.

2.5.4. Added Mass

As a rigid body moves through a fluid, there are pressure-induced forces separate from drag associated with how the body is required to accelerate the surrounding fluid during unsteady motion. This is called “added mass” and is a function of the geometry of the vehicle. Though these parameters are typically ignored in aerial applications due to the low density of air, they must be accounted for in underwater analyses since the

density of the fluid is much higher and on the same order as that of the rigid body. The forces and moments are expressed as described in [13]

$$F_j = -\dot{U}_i m_{ij} - \varepsilon_{jkl} U_i \omega_k m_{li} \quad (9a)$$

$$M_j = -\dot{U}_i m_{j+3,i} - \varepsilon_{jkl} U_i \omega_k m_{l+3,i} - \varepsilon_{jkl} U_k U_i m_{li} \quad (9b)$$

where j denotes the direction of the force, i=1, 2, 3, 4, 5, 6 and j, k, l = 1, 2, 3. ε_{jkl} is the alternating tensor where

$$\varepsilon_{jkl} = \begin{cases} 0; & \text{if any pair of the indices j, k, l are equal} \\ 1; & \text{if j, k, l are in cyclic order} \\ -1; & \text{if j, k, l are in anti - cyclic order} \end{cases} \quad (10)$$

The overall effect of this added mass is more commonly condensed into an symmetrical added mass or inertia matrix using Society of Naval Architects and Marine Engineers (SNAME) notation [14] as

$$M_A = \begin{bmatrix} X_{\dot{u}} & X_{\dot{v}} & X_{\dot{w}} & X_{\dot{p}} & X_{\dot{q}} & X_{\dot{r}} \\ Y_{\dot{u}} & Y_{\dot{v}} & Y_{\dot{w}} & Y_{\dot{p}} & Y_{\dot{q}} & Y_{\dot{r}} \\ Z_{\dot{u}} & Z_{\dot{v}} & Z_{\dot{w}} & Z_{\dot{p}} & Z_{\dot{q}} & Z_{\dot{r}} \\ K_{\dot{u}} & K_{\dot{v}} & K_{\dot{w}} & K_{\dot{p}} & K_{\dot{q}} & K_{\dot{r}} \\ M_{\dot{u}} & M_{\dot{v}} & M_{\dot{w}} & M_{\dot{p}} & M_{\dot{q}} & M_{\dot{r}} \\ N_{\dot{u}} & N_{\dot{v}} & N_{\dot{w}} & N_{\dot{p}} & N_{\dot{q}} & N_{\dot{r}} \end{bmatrix} \quad (11)$$

Overall, the expanded equations for forces and moments on the rigid body due to the added mass terms can be expressed as derived by Imlay [15],

$$\begin{aligned} X_A = & X_{\dot{u}}\dot{u} + X_{\dot{w}}(\dot{w} + uq) + X_{\dot{q}}\dot{q} + Z_{\dot{w}}wq + Z_{\dot{q}}q^2 \\ & + X_{\dot{v}}\dot{v} + X_{\dot{p}}\dot{p} + X_{\dot{r}}\dot{r} - Y_{\dot{v}}vr - Y_{\dot{p}}rp - Y_{\dot{r}}r^2 \\ & - X_{\dot{v}}ur - Y_{\dot{w}}wr \\ & + Y_{\dot{w}}vq + Z_{\dot{p}}pq - (Y_{\dot{q}} - Z_{\dot{r}})qr \end{aligned} \quad (12a)$$

$$\begin{aligned}
Y_A &= X_{\dot{v}}\dot{u} + Y_{\dot{w}}\dot{w} + Y_{\dot{q}}\dot{q} \\
&+ Y_{\dot{v}}\dot{v} + Y_{\dot{p}}\dot{p} + Y_{\dot{r}}\dot{r} + X_{\dot{v}}vr - Y_{\dot{w}}vp + X_{\dot{r}}r^2 + (X_{\dot{p}} - Z_{\dot{r}})rp - Z_{\dot{p}}p^2 \\
&- X_{\dot{w}}(up - wr) + X_{\dot{u}}ur - Z_{\dot{w}}wp \\
&- Z_{\dot{q}}pq + X_{\dot{q}}qr
\end{aligned} \tag{12b}$$

$$\begin{aligned}
Z_A &= X_{\dot{w}}(\dot{u} - wq) + Z_{\dot{w}}\dot{w} + Z_{\dot{q}}\dot{q} - X_{\dot{u}}uq - X_{\dot{q}}q^2 \\
&+ Y_{\dot{w}}\dot{v} + Z_{\dot{p}}\dot{p} + Z_{\dot{r}}\dot{r} + Y_{\dot{v}}vp + Y_{\dot{r}}rp + Y_{\dot{p}}p^2 \\
&+ X_{\dot{v}}up + Y_{\dot{w}}wp \\
&- X_{\dot{v}}vq - (X_{\dot{p}} - Y_{\dot{q}})pq - X_{\dot{r}}qr
\end{aligned} \tag{12c}$$

$$\begin{aligned}
K_A &= X_{\dot{p}}\dot{u} + Z_{\dot{p}}\dot{w} + K_{\dot{q}}\dot{q} - X_{\dot{v}}wu + X_{\dot{r}}uq - Y_{\dot{w}}w^2 - (Y_{\dot{q}} - Z_{\dot{r}})wq + M_{\dot{r}}q^2 \\
&+ Y_{\dot{p}}\dot{v} + K_{\dot{p}}\dot{p} + K_{\dot{r}}\dot{r} + Y_{\dot{w}}v^2 - (Y_{\dot{q}} - Z_{\dot{r}})vr + Z_{\dot{p}}vp - M_{\dot{r}}r^2 - K_{\dot{q}}rp \\
&+ X_{\dot{w}}uv - (Y_{\dot{v}} - Z_{\dot{w}})vw - (Y_{\dot{r}} + Z_{\dot{q}})wr - Y_{\dot{p}}wp - X_{\dot{q}}ur \\
&+ (Y_{\dot{r}} + Z_{\dot{q}})vq + K_{\dot{r}}pq - (M_{\dot{q}} - N_{\dot{r}})qr
\end{aligned} \tag{12d}$$

$$\begin{aligned}
M_A &= X_{\dot{q}}(\dot{u} + wq) + Z_{\dot{q}}(\dot{w} - uq) + M_{\dot{q}}\dot{q} - X_{\dot{w}}(u^2 - w^2) - (Z_{\dot{w}} - X_{\dot{u}})wu \\
&+ Y_{\dot{q}}\dot{v} + K_{\dot{q}}\dot{p} + M_{\dot{r}}\dot{r} + Y_{\dot{p}}vr - Y_{\dot{r}}vp - K_{\dot{r}}(p^2 - r^2) + (K_{\dot{p}} - N_{\dot{r}})rp \\
&- Y_{\dot{w}}uv + X_{\dot{v}}vw - (X_{\dot{r}} + Z_{\dot{p}})(up - wr) + (X_{\dot{p}} - Z_{\dot{r}})(wp + ur) \\
&- M_{\dot{r}}pq + K_{\dot{q}}qr
\end{aligned} \tag{12e}$$

$$\begin{aligned}
N_A &= X_{\dot{r}}\dot{u} + Z_{\dot{r}}\dot{w} + M_{\dot{r}}\dot{q} + X_{\dot{v}}u^2 + Y_{\dot{w}}wu - (X_{\dot{p}} - Y_{\dot{q}})uq - Z_{\dot{p}}wq - K_{\dot{q}}q^2 \\
&+ Y_{\dot{r}}\dot{v} + K_{\dot{r}}\dot{p} + N_{\dot{r}}\dot{r} - X_{\dot{v}}v^2 - X_{\dot{r}}vr - (X_{\dot{p}} - Y_{\dot{q}})vp + M_{\dot{r}}rp + K_{\dot{q}}p^2 \\
&- (X_{\dot{u}} - Y_{\dot{v}})uv - X_{\dot{w}}vw + (X_{\dot{q}} + Y_{\dot{p}})up + Y_{\dot{r}}ur + Z_{\dot{q}}wp \\
&- (X_{\dot{q}} + Y_{\dot{p}})vq - (K_{\dot{p}} - M_{\dot{q}})pq - K_{\dot{r}}qr
\end{aligned} \tag{12f}$$

The equations were formatted by Imlay [15] so that the longitudinal components are on the first line, lateral components are on the second line, mixed terms involving u or w are on the third line, and mixed second order terms that are sometimes neglected are placed on the fourth line.

2.5.5. Hydrodynamic Damping

The final set of forces being considered in this analysis is the hydrodynamic damping forces. The main damping force is the viscous damping force due to vortex shedding, given by the general equation

$$F_D = -\frac{1}{2}\rho C_D(R_n)A|u|u \quad (13)$$

where ρ is the fluid density, C_D is the coefficient of drag that is dependent upon the Reynolds number, R_n , A is the corresponding reference area to the applied coefficient of drag, and u is the velocity of the vehicle. The equation for the Reynolds number of a given geometry is

$$R_n = \frac{uD}{\nu} \quad (14)$$

where D is the characteristic length of the geometry and ν (“nu”, not “v”) is the kinematic viscosity for the surrounding fluid [16].

The drag on a body rotating in a fluid can be related to the linear damping using the following equation

$$\omega \cdot r = u \quad (15)$$

where ω is the instantaneous angular velocity of the rotating body, and r is the distance from the axis of rotation to a specific cross section of the body. In this case, the

corresponding linear force would be multiplied by that same distance from the axis of rotation to obtain the moment. This moment arm must be integrated due to the fact that each successive cross section of a body with a given damping coefficient may lie a different distance away from the axis of rotation.

Overall, the drag moment can be approximated as

$$\begin{aligned}
 M_D &= \int (F_D \perp r) = -\frac{1}{2} \rho C_D (R_n) \int_{r_1}^{r_2} (b \cdot dr) \cdot |\omega \cdot r| \cdot (\omega \cdot r) \cdot r \\
 &= -\frac{1}{2} \rho C_D (R_n) b |\omega| \omega \cdot \int_{r_1}^{r_2} r^2 |r| dr
 \end{aligned} \tag{16}$$

where the variable “b” is introduced to represent the reference area length of each successive cross section that is parallel to the axis of rotation. An example of this is given in the diagram below in Fig. 6 for a rectangular prism of square cross section being rotated about its end. It should be noted that some of the general dynamics nomenclature when addressing damping equations overlaps with that addressing the other marine dynamics nomenclature, such as “r”. The notation with hydrodynamic damping can be considered isolated from other nomenclature unless specifically noted in the text.

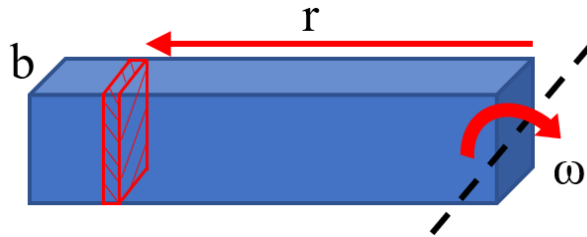


Figure 6: Example of notation for rectangular prism of square cross section rotating about one end (rotation about the dashed line).

Where the damping due to vortex shedding, or pressure drag, often uses the reference area of the body perpendicular to the flow, nonlinear skin friction across the

surface area of the vehicle is also taken into account. This is notated with a skin friction coefficient of drag using equation 13, with C_F instead of C_D . There can also be lift forces associated with vortex shedding, especially with streamlined bodies or ones generally shaped as airfoils [16]. With the many irregularities on LoCO's surface, it is generally not being considered a streamlined body and it is assumed that any lift forces generated by the vehicle are negligible in comparison to drag forces.

The non-velocity terms are typically condensed into a single coefficient, with the subscript indicating the direction of motion causing the force. Also due to asymmetry, there will be a net pitching moment generated by linear movement in the vertical direction, and a net yawing moment generated by linear movement in the lateral direction. Overall, the expanded equations for forces and moments on the rigid body due to the hydrodynamic damping terms [17] can be expressed as

$$X_D = X_{u|u}|u|u| \quad (17a)$$

$$Y_D = Y_{v|v}|v|v| \quad (17b)$$

$$Z_D = Z_{w|w}|w|w| \quad (17c)$$

$$K_D = K_{p|p}|p|p| \quad (17d)$$

$$M_D = M_{q|q}|q|q| + M_{w|w}|w|w| \quad (17e)$$

$$N_D = N_{r|r}|r|r| + N_{v|v}|v|v| \quad (17f)$$

2.6. Overall Kinetics Equations

Tying together each of the force and moment components acting on the AUV,

$$X = X_P + X_R + X_D - X_A \quad (18a)$$

$$Y = Y_P + Y_R + Y_D - Y_A \quad (18b)$$

$$Z = Z_P + Z_R + Z_D - Z_A \quad (18c)$$

$$K = K_P + K_R + K_D - K_A \quad (18d)$$

$$M = M_P + M_R + M_D - M_A \quad (18e)$$

$$N = N_P + N_R + N_D - N_A \quad (18f)$$

2.7. Conclusion

In this chapter, a body-fixed reference frame is defined for the underwater vehicle and parameters for motion along these body axes are related back to the overall inertial frame. The 6-degrees-of-freedom equations of motion for such a rigid body are listed. External force and moment equations are addressed for environmental forces, propulsion, restoring forces, added mass, and drag. Assumptions being applied to the dynamic analysis of LoCO are explained with the corresponding type of external force.

Chapter 3

Estimation of LoCO Dynamic Parameters

3.1. Introduction

Now that the governing dynamic equations have been established for LoCO, the various constants related to the underwater vehicle must be determined. The general derivation of each parameter is given in each section, but in an effort to maintain the most accurate approximations possible, most simplifying assumptions are left to the end of each section in order to validate those assumptions. A majority of the external and internal components of LoCO are modeled in a Computer-Aided Design (CAD) program called SolidWorks. Ballasting is excluded from this modeling. Overall, a combination of physical measurements, analytical formulas, and SolidWorks measurements are used to estimate these parameters.

3.2. Buoyancy

One of the foundational parameters for an underwater vehicle is its buoyancy. The overall buoyancy is determined as the equivalent weight of fluid that is occupied by the vehicle when underwater. The density of water is assumed to be approximately 1000 kg/m³ throughout the estimation of parameters. Gravity is assumed to be 9.80665 m/s² throughout the estimation as well. Also, the center of buoyancy needs to be calculated in relation to the body frame origin. For a composite body such as LoCO, this is done by using the center of buoyancy and volume of each component

$$\mathbf{CB} = \frac{\sum_{i=1}^n \mathbf{CB}_i \cdot V_i}{\sum_{i=1}^n V_i} \quad (19)$$

where \mathbf{CB} denotes the center of buoyancy position vector, V is the volume, and the summations are taken for each contributing component of LoCO.

A comprehensive table of components with their corresponding center of buoyancy and volume used to equate the overall buoyancy for the vehicle can be found in Table 9 in Appendix A. For simple shapes like the main tubes or the tube penetrators approximated as solid cylinders, the volume and center of buoyancy were determined analytically according to their positions in the CAD model. For more complicated shapes such as the clamp connectors or the thrusters, the SolidWorks Mass Analysis tool allows for an automated computation of total volume and center of buoyancy. The center of buoyancy in this case is equivalent to the center of gravity of the object assuming constant density, which is valid since the geometries are displacing a fluid of constant density. Overall, Table 1 below gives the summary of this analysis.

Parameter Description	Variable	Value	Units
Water Density	ρ	1000	kg/m ³
Vehicle Displacement Volume	V	0.012545	m ³
Buoyancy Force	B	123.02	N
Center of Buoyancy	\mathbf{CB}_x	0.2417	m
	\mathbf{CB}_y	-4.836E-09	m
	\mathbf{CB}_z	5.166E-05	m

Table 1: Vehicle buoyancy analysis summary.

For the purpose of simplifying the governing dynamic equation for LoCO, the small values for the y and z positions of the center of buoyancy can be assumed to be 0 from this analysis.

3.3. Mass and Moments of Inertia

Next, the mass and moments of inertia for LoCO must be approximated. The moments of inertia and center of mass location for LoCO are calculated based on placing the body-fixed coordinate frame origin centrally between the rear faces of each tube as described in section 2.2. To accomplish this, the same previous component matrix comprised of 67 items is used and can be found in Table 9 of Appendix A.

Where possible, such as with the Pixhawk inertial measurement unit, Blue Robotics components, and the batteries, component masses were obtained from vendor sites. For the polycarbonate tubes, 3D-printed components, and ballast weights, manual mass measurements were taken. Due to their relatively insignificant masses, 3D-printed components smaller than the clamp connectors bridging the two polycarbonate tubes were neglected. With how LoCO is manually ballasted in order to maintain neutral buoyancy with the equipment currently onboard and checked with each field deployment, the location and number of ballasts are not maintained within the CAD model. Though not displayed, the ballasts are still taken into account and listed in the component matrix. Other items assumed to be negligible relative to the overall mass of the vehicle are the cameras, electrical wires and connections, the reed switch, bolts, and nuts. The mass for each medium-density fiber mounting board was approximated based on its volume obtained from the SolidWorks Mass Analysis tool and an average density of the material [18]. The mass approximation for each penetrator was made similarly based on their volume and the density of Aluminum T6061 [19].

For geometric approximations of center of gravity and moments of inertia, the batteries, ballast weights, and internal computational and power components are

approximated as rectangular prisms. The tubes and tube clamp sets are approximated as hollow cylinders. The moments of inertia for these two shapes are given in the diagram below in Fig. 7 [20]. For the remaining components of more complex geometries, the SolidWorks Mass Analysis tool is used to compute the center of gravity and moments of inertia of each component assuming constant density.

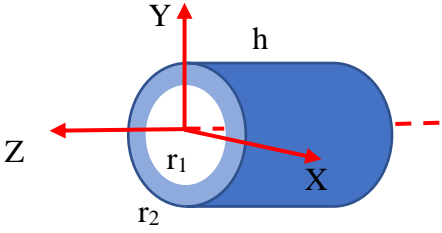
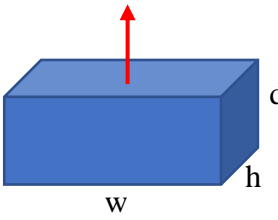
	
<p style="text-align: center;">Hollow Cylinder</p> $I_z = 1/2 m (r_1^2 + r_2^2) \quad (20a)$ $I_x = I_y = 1/12 m (3(r_1^2 + r_2^2) + h^2) \quad (20b)$ <p>where r1 is inner radius, r2 is outer radius, and h is height.</p>	<p style="text-align: center;">Rectangular Prism</p> $I_d = 1/12 m (h^2 + w^2) \quad (21)$

Figure 7: Moments of inertia for hollow cylinder and rectangular prism [20].

To determine the composite moments of inertia for the underwater vehicle, the moments of inertia for each component are required to be translated into the body-fixed coordinate frame. This can be done using the parallel-axis theorem for moments of inertia. An example of this for translating these component inertias into the body frame so they can be summed into the total vehicle moments of inertia are given below.

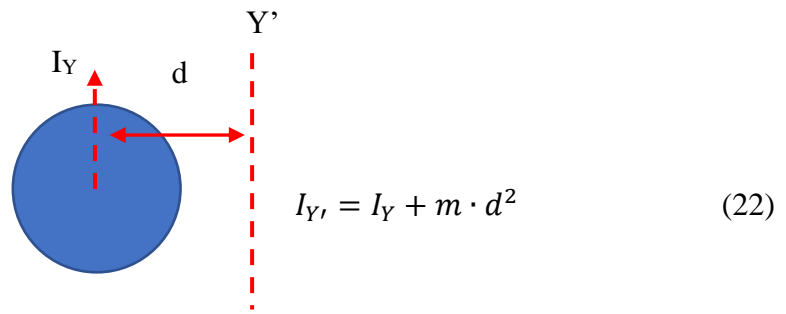


Figure 8: Parallel axis theorem example, where m is mass of the object.

Similar to the buoyancy analysis, the full component matrix is not included directly in the text, but a summary of results is given below in Table 2.

Parameter Description	Variable	Value	Units
Mass	m	12.320	kg
Weight	W	120.82	N
Center of Gravity	CG_x	0.2538	m
	CG_y	0.0010191	m
	CG_z	0.002130	m
Moments of Inertia	I_x	0.19094	kg m^2
	I_y	1.2050	kg m^2
	I_z	1.3465	kg m^2
	I_{xy}	0.002257	kg m^2
	I_{yz}	-0.0002695	kg m^2
	I_{xz}	0.005911	kg m^2

Table 2: Vehicle mass and moments of inertia analysis summary.

The results of this analysis serve to validate a number of dynamic assumptions. The estimated weight of the vehicle is only approximately 2 N less than the buoyancy force. For a neutrally buoyant vehicle where theoretically, these values are equal, this shows that the components ignored in the mass analysis were indeed negligible. For the center of gravity estimate, relative to the center of buoyancy calculated in the previous analysis, the center of gravity is shifted by approximately 1 cm in the x direction, 1 mm

in the y direction, and 2 mm in the z direction. As mentioned in Chapter 2, it is often desired to design and ballast underwater vehicles so that the center of buoyancy is located directly above the center of gravity when the vehicle is in a stationary horizontal, flat position. The mass analysis appears to corroborate this desired stability design in LoCO as well. Since the displacements from the center of buoyancy are so small relative to the overall vehicle, and it has been observed in field trials that LoCO does maintain a stable, flat position in water, it can be approximated that the center of gravity is equal to the established center of buoyancy that is likely to be much more accurate than the sum of mass approximations.

For the moments of inertia of the vehicle, the moment of inertia in the x direction is lower than the other principal moments of inertia as expected due to the more elongated nature of LoCO's design. From the location of the coordinate frame origin, there is an observable geometric symmetry in the x-z and x-y planes. With the design and ballasting of LoCO, if the symmetries were to hold true for the mass distribution of the vehicle, the products of inertia would all be equal to 0. Due to the small values of the products of inertia, this can be assumed the case for LoCO and further simplifies the governing dynamic equations.

3.4. Added Mass Coefficients

For surface vessels and more complex analyses of ship dynamics, the estimation of added mass parameters for vehicles is done using computational methods. If solving for added mass analytically such as in this thesis, the two most common ways of doing this are approximating the shape of the underwater vehicle as an ellipsoid or using a

method known as “strip theory”. Strip theory employs the use of solutions for the added mass of 2-dimensional shapes and integrates the results into three dimensions. This section on added mass uses external computational findings and strip theory to approximate the added mass coefficients for LoCO.

Analytical estimation of these parameters requires a simplification of the underwater vehicle geometry. Overall, the geometries included are for the tubes, thrusters, clamp connectors, and backbone. Three different models were created for assessing the added mass of the vehicle since in certain directions of motion, certain components are removed. These approximations are done in order to best approximate and not over-estimate the added mass of the vehicle, as each added mass approximation is technically that of an independent three-dimensional object. For example, in forward motion, the forward clamp connector resides in the wake of the fluid flowing over the vertical thruster and not in an open fluid, so its actual contribution to added mass is assumed to be negligible. The geometric approximations for each linear direction of travel are given below in Figs. 9-11.

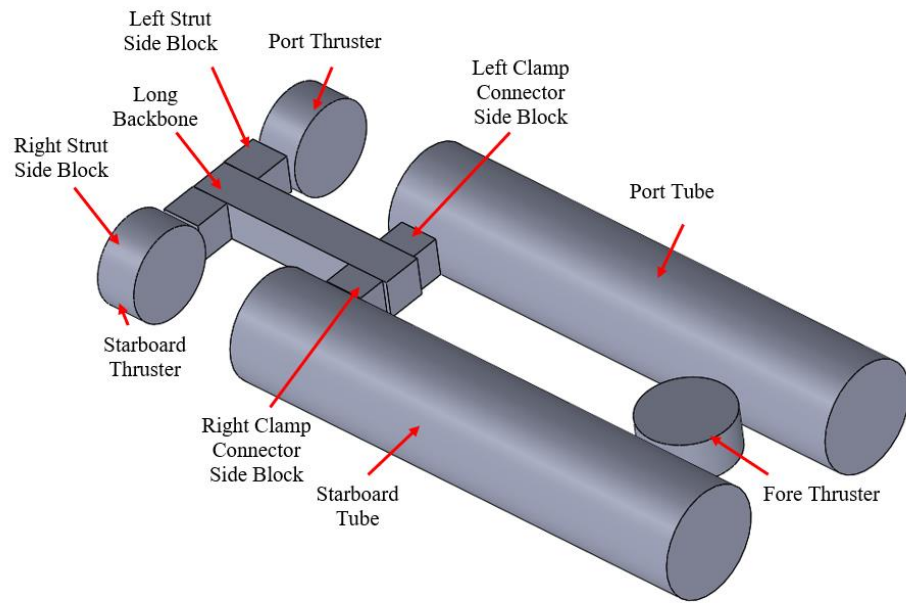


Figure 9: Geometric approximation for LoCO flow in x-direction – “X-Model”.

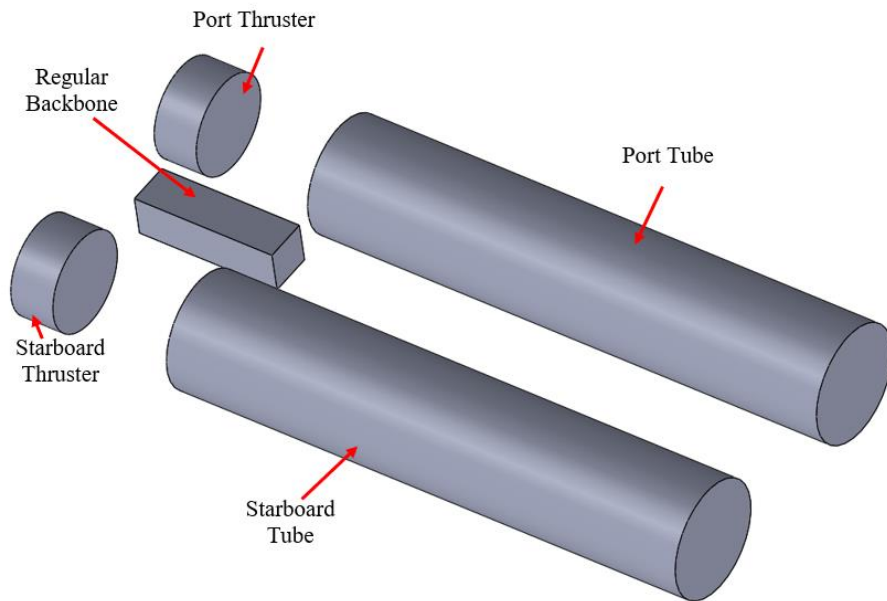


Figure 10: Geometric approximation for LoCO flow in y-direction – “Y-Model”.

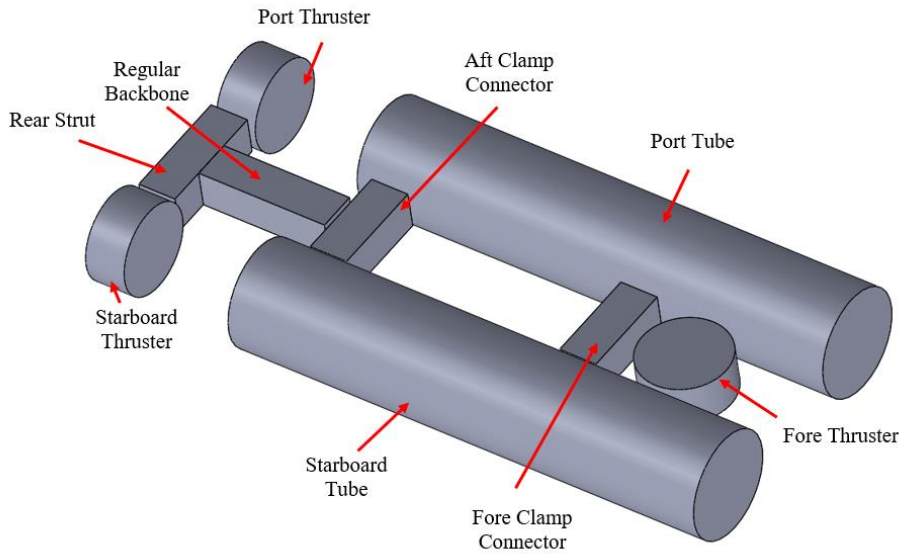


Figure 11: Geometric approximation for LoCO flow in z -direction – “Z-Model”.

Component	Variable
Port Tube	tube
Starboard Tube	
Port Thruster	aft_thruster
Starboard Thruster	
Fore Thruster	fore_thruster
Fore Clamp Connector	fore_connector
Aft Clamp Connector	aft_connector
Regular Backbone	backbone
Long Backbone	long_backbone
Rear Strut	strut
Left Strut Side Block	strut_side
Right Strut Side Block	
Left Clamp Connector Side Block	clamp_side
Right Clamp Connector Side Block	

Table 3: Table of components and corresponding variable names for geometric LoCO models.

Beginning with specifics for the added mass of the vehicle, the two types of cross sections involved in the models are circles and squares. The added mass components for

these shapes in 2D are readily available in sources such as [13], [21] and are given in the diagram below in Fig. 12.

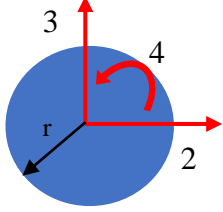
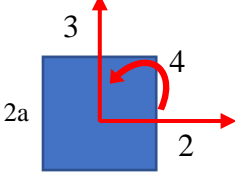
	
Circle	Square
$a_{22} = a_{33} = \pi \rho r^2$ (23a) $a_{44} = 0$ (23b)	$a_{22} = a_{33} = 1.51 \rho \pi a^2$ (24a) $a_{44} = 0.234 \rho \pi a^4$ (24b)
where ρ is the surrounding fluid density.	where ρ is the surrounding fluid density.

Figure 12: Added mass parameters for a circle and a square [13], [21].

Using SNAME's Principles of Naval Architecture [14], [22] notation for added mass, for a 3D object, the symmetric added mass matrix previously established can also be notated as

$$\begin{bmatrix} X_{\dot{u}} & X_{\dot{v}} & X_{\dot{w}} & X_{\dot{p}} & X_{\dot{q}} & X_{\dot{r}} \\ Y_{\dot{u}} & Y_{\dot{v}} & Y_{\dot{w}} & Y_{\dot{p}} & Y_{\dot{q}} & Y_{\dot{r}} \\ Z_{\dot{u}} & Z_{\dot{v}} & Z_{\dot{w}} & Z_{\dot{p}} & Z_{\dot{q}} & Z_{\dot{r}} \\ K_{\dot{u}} & K_{\dot{v}} & K_{\dot{w}} & K_{\dot{p}} & K_{\dot{q}} & K_{\dot{r}} \\ M_{\dot{u}} & M_{\dot{v}} & M_{\dot{w}} & M_{\dot{p}} & M_{\dot{q}} & M_{\dot{r}} \\ N_{\dot{u}} & N_{\dot{v}} & N_{\dot{w}} & N_{\dot{p}} & N_{\dot{q}} & N_{\dot{r}} \end{bmatrix} = \begin{bmatrix} A_{11} & A_{12} & A_{13} & A_{14} & A_{15} & A_{16} \\ A_{21} & A_{22} & A_{23} & A_{24} & A_{25} & A_{26} \\ A_{31} & A_{32} & A_{33} & A_{34} & A_{35} & A_{36} \\ A_{41} & A_{42} & A_{43} & A_{44} & A_{45} & A_{46} \\ A_{51} & A_{52} & A_{53} & A_{54} & A_{55} & A_{56} \\ A_{61} & A_{62} & A_{63} & A_{64} & A_{65} & A_{66} \end{bmatrix} \quad (25)$$

where the first subscript denotes the direction of the added mass, and the second subscript denotes the motion direction causing that added mass. In order to first decrease the scope of the analysis, some important simplifications can be made. It has already been established that LoCO has planes of symmetry in the x-z plane and the x-y plane. This allows many of the off-diagonal elements to be set to 0:

$$M_A = \begin{bmatrix} X_{\dot{u}} & 0 & 0 & 0 & 0 & 0 \\ 0 & Y_{\dot{v}} & 0 & 0 & 0 & Y_{\dot{r}} \\ 0 & 0 & Z_{\dot{w}} & 0 & Z_{\dot{q}} & 0 \\ 0 & 0 & 0 & K_{\dot{p}} & 0 & 0 \\ 0 & 0 & M_{\dot{w}} & 0 & M_{\dot{q}} & 0 \\ 0 & N_{\dot{v}} & 0 & 0 & 0 & N_{\dot{r}} \end{bmatrix} \quad (26)$$

Again from the Principles of Naval Architecture [22], these 3D coefficients can be obtained from the 2D added mass parameters integrated over the length of the object,

$$A_{11} = \int a_{11} dx \quad (27a)$$

$$A_{22} = \int a_{22} dx \quad (27b)$$

$$A_{33} = \int a_{33} dx \quad (27c)$$

$$A_{44} = \int a_{44} dx \quad (27d)$$

$$A_{55} = \int x^2 a_{33} dx \quad (27e)$$

$$A_{66} = \int x^2 a_{22} dx \quad (27f)$$

$$A_{26} = A_{62} = \int x a_{22} dx \quad (27g)$$

$$A_{35} = A_{53} = - \int x a_{33} dx \quad (27h)$$

Though strip theory makes evaluating added mass parameters in cross flow possible, axial flow against these cross sections does not have the same sort of available solutions. One way of estimating this axial added mass due to acceleration along the same axis is using the approximation for a streamlined body, where such an added mass is approximately 5 to 10 percent of the mass of the displaced fluid. However, LoCO cannot necessarily be assumed to be a streamlined body, especially taking the individual added mass of each thruster into account where those cylinder approximations are more related to a bluff body.

A solution to this is provided in [23]. In the thesis, computational simulations are performed for various cylinder geometries in axial flow to investigate the added mass of each shape. Equation 5.2 in this paper provides a regression line equation fitting data for cylinders with length over diameter ratios from approximately 0.025 to 4. Adapting the notation to match this thesis,

$$X_{\ddot{u}} = A_{11} = 0.57 \left(\frac{H}{D} \right)^{-0.93} \cdot \rho V \quad (28)$$

where H is the height of the cylinder, D is the diameter, ρ is the surrounding fluid density, and V is the volume of the cylinder. Also according to [21], a reasonable estimate for the added mass of a square cross section is with a circle cross section where the diameter is approximately 1.224 times the side length so that it effectively “rounds out” the square.

Now that the general form for added mass coefficients has been established, the models for LoCO can begin to be analyzed. First for the surge added mass coefficient due to surge acceleration based on the X-Model,

$$\begin{aligned} X_{\ddot{u}} = A_{11} = & \rho \cdot \left(2 \cdot 0.57 \left(\frac{H_{tube}}{D_{tube}} \right)^{-0.93} V_{tube} \right) \dots \\ & + \left(2 \cdot 0.57 \left(\frac{H_{rear_thruster}}{D_{rear_thruster}} \right)^{-0.93} V_{rear_thruster} \right) \dots \\ & + \left(0.57 \left(\frac{H_{long_back}}{1.2244 \cdot D_{long_back}} \right)^{-0.93} V_{long_back} \right) + \left(2 \cdot \frac{1.51\pi}{4} \cdot V_{clamp_side} \right) \dots \\ & + \left(2 \cdot \frac{1.51\pi}{4} \cdot V_{strut_side} \right) + V_{fore_thruster} \end{aligned} \quad (29)$$

where V is volume.

Then for the sway added mass due to sway acceleration based on the Y-Model,

$$Y_{\ddot{v}} = A_{22} = \rho \cdot \left((2 \cdot V_{tube}) + (2 \cdot V_{rear_thruster}) + \left(\frac{1.51\pi}{4} \cdot V_{backbone} \right) \right) \quad (30)$$

and for the heave added mass due to heave acceleration based on the Z-Model,

$$\begin{aligned}
Z_{\dot{w}} = A_{33} = & \rho \cdot ((2 \cdot V_{tube}) + (2 \cdot V_{rear_thruster}) + \left(\frac{1.51\pi}{4} \cdot V_{backbone}\right) \dots \\
& + \left(\frac{1.51\pi}{4} \cdot V_{fore_connector}\right) + \left(\frac{1.51\pi}{4} \cdot V_{aft_connector}\right) \dots \\
& + \frac{1.51\pi}{4} \cdot V_{strut} + \left(0.57 \left(\frac{H_{rear_thruster}}{D_{rear_thruster}}\right)^{-0.93} V_{thruster}\right) \quad (31)
\end{aligned}$$

For the roll added mass coefficient due to roll acceleration, the Z-Model is used since roll motion offset from the central axis leads to dealing with instantaneous vertical motion of the individual components. For the backbone, there is already a coefficient a_{44} that can be applied and integrated over the backbone. For the connectors, strut, and vertical thruster, roll for the overall underwater vehicle can be expressed equivalent to pitch about the central axis for each of the components, leading to using equation 27e as $\int_{-Length/2}^{Length/2} x^2 a_{33} dx$. The roll added mass for the tubes and rear thrusters can account for their offset from the roll axis with an appropriate modification of equation 27d, similar to that of equation 27e,

$$A_{44} = \int r^2 a_{33} dx \quad (32)$$

where r, in this case, is the perpendicular distance from the central axis to the center of the cylinders. Using these expressions then,

$$\begin{aligned}
K_{\dot{p}} = A_{44} = & \rho \cdot ((2 \cdot y c_{tube}^2 \cdot V_{tube}) + (2 \cdot y c_{rear_thruster}^2 \cdot V_{rear_thruster}) \dots \\
& + \left(\frac{H_{fore_thruster}^2}{12} \cdot V_{fore_thruster}\right) + \left(\frac{1.51\pi}{4} \cdot V_{fore_connector}\right) + \left(\frac{1.51\pi}{4} \cdot V_{aft_connector}\right) \dots \\
& + \left(\frac{1.51\pi}{4} \cdot V_{strut} \cdot \frac{length_{strut}^2}{12}\right) + \frac{0.234\pi}{4} \cdot \left(\frac{width_{backbone}}{2}\right)^2 \cdot V_{backbone} \quad (33)
\end{aligned}$$

where y_c is the geometric center offset in the y direction, length is the length along the longest axis of the component, and width is the side length of the square cross section.

For the pitch added mass coefficient due to pitch acceleration, the Z-Model is the most accurate to use again. The added mass coefficients for the tubes, rear thrusters, and backbone can be determined using the basic formula in equation 27e. For the vertical thruster, clamp connectors, and rear strut, a modified version of the same equation must be used considering cross-section propagation is a constant perpendicular distance from the axis of rotation:

$$A_{55} = r^2 \int a_{33} dx \quad (34)$$

where r in this case is again the perpendicular distance from the axis of rotation to the corresponding centerline of the rotating component. Overall, then,

$$\begin{aligned} M_{\dot{q}} = A_{55} = & \rho \cdot \left(2 \cdot \frac{(x_{2tube}^3 - x_{1tube}^3)}{3} \cdot S_{tube} \right) \dots \\ & + \left(2 \cdot \frac{(x_{2rear_thruster}^3 - x_{1rear_thruster}^3)}{3} \cdot S_{rear_thruster} \right) \dots \\ & + \left(0.57 \left(\frac{H_{thruster}}{D_{thruster}} \right)^{-0.93} \cdot x_{c_{fore_thruster}}^2 \cdot V_{fore_thruster} \right) \dots \\ & + \left(\frac{1.51\pi}{4} \cdot x_{c_{fore_connector}}^2 \cdot V_{fore_connector} \right) + \left(\frac{1.51\pi}{4} \cdot x_{c_{aft_connector}}^2 \cdot V_{aft_connector} \right) \dots \\ & + \left(\frac{1.51\pi}{4} \cdot x_{c_{strut}}^2 \cdot V_{strut} \right) + \left(\frac{(x_{2backbone}^3 - x_{1backbone}^3)}{3} \cdot S_{backbone} \right) \end{aligned}$$

where S denotes the cross-sectional reference area, x_c is the is the geometric center offset in the x direction, and x_1 and x_2 represent the limits of integration performed in the x direction (from x_1 to x_2).

For the yaw added mass due to yaw acceleration, the Y-Model is utilized. Though some components are offset in both the x and y directions, it is assumed that

instantaneously, crossflow over the geometry due to yaw is in the y direction since components are generally more offset from the origin in the x direction than the y direction. All components for the yaw added mass are computed this way.

$$\begin{aligned}
N_{\dot{r}} = A_{66} = \rho \cdot & \left(2 \cdot \frac{(x_{2tube}^3 - x_{1tube}^3)}{3} \cdot S_{tube} \right) \dots \\
& + \left(2 \cdot \frac{(x_{2rear_thruster}^3 - x_{1rear_thruster}^3)}{3} \cdot S_{rear_thruster} \right) \dots \\
& + \left(\frac{(x_{2backbone}^3 - x_{1backbone}^3)}{3} \cdot S_{backbone} \right) \quad (35)
\end{aligned}$$

Now, the off-diagonal elements must be formulated. For the yaw added mass due to sway acceleration and sway added mass due to yaw acceleration,

$$\begin{aligned}
Y_{\dot{r}} = N_{\dot{v}} = A_{26} = \rho \cdot & \left(2 \cdot \frac{(x_{2tube}^2 - x_{1tube}^2)}{2} \cdot S_{tube} \right) \dots \\
& + \left(2 \cdot \frac{(x_{2rear_thruster}^2 - x_{1rear_thruster}^2)}{2} \cdot S_{rear_thruster} \right) \dots \\
& + \left(\frac{(x_{2backbone}^2 - x_{1backbone}^2)}{2} \cdot S_{backbone} \right) \quad (36)
\end{aligned}$$

and with a similar derivation for the heave added mass due to pitch acceleration and pitch added mass due to heave acceleration,

$$\begin{aligned}
Z_{\dot{q}} = M_{\dot{w}} = A_{35} = \rho \cdot & \left(2 \cdot \frac{(x_{2tube}^2 - x_{1tube}^2)}{2} \cdot S_{tube} \right) \dots \\
& + \left(2 \cdot \frac{(x_{2rear_thruster}^2 - x_{1rear_thruster}^2)}{2} \cdot S_{thruster} \right) \dots \\
& + \left(0.57 \left(\frac{H_{thruster}}{D_{thruster}} \right)^{-0.93} \cdot x_{C_{fore_thruster}} \cdot V_{rear_thruster} \right) \dots \\
& + \left(\frac{1.51\pi}{4} \cdot x_{C_{fore_connector}} \cdot V_{fore_connector} \right) + \left(\frac{1.51\pi}{4} \cdot x_{C_{aft_connector}} \cdot V_{aft_connector} \right) \dots \\
& + \left(\frac{1.51\pi}{4} \cdot x_{C_{strut}} \cdot V_{strut} \right) + \left(\frac{(x_{2backbone}^2 - x_{1backbone}^2)}{2} \cdot S_{backbone} \right) \quad (37)
\end{aligned}$$

Inserting values and solving for each of the parameters gives the following displayed in Table 4.

Parameter Description	Variable	Value	Units
Water Density	ρ	1000	kg/m ³
Added Mass	$X_{\dot{u}}$	2.899	kg
	$Y_{\dot{v}}$	11.855	kg
	$Z_{\dot{w}}$	12.915	kg
	$K_{\dot{p}}$	0.13557	kg m ²
	$M_{\dot{q}}$	1.4260	kg m ²
	$N_{\dot{r}}$	1.0667	kg m ²
	$Z_{\dot{q}}$	-3.562	kg m
	$M_{\dot{w}}$	-3.562	kg m
	$Y_{\dot{r}}$	2.818	kg m
	$N_{\dot{v}}$	2.818	kg m

Table 4: Added mass analysis values.

3.5. Hydrodynamic Damping Coefficients

The first step in determining the hydrodynamic damping parameters on the underwater vehicle is to determine the relevant coefficients of drag for each geometric shape involved. Similar to the added mass, in order to analytically approximate the composite damping coefficients for the vehicle, geometric assumptions must be made. The X-Model, Y-Model, and Z-Model are used in this analysis as they were with the added mass.

With a forward top speed of approximately 1.5 meters per second, an overall length of 0.73 meters, and with the kinematic viscosity of water at 20 degrees Celsius as $1.004 \cdot 10^{-6} \text{ m}^2/\text{s}$ [24], the overall Reynolds number of LoCO in forward motion is

$$R_n = \frac{uD}{\nu} = \frac{1.5 \cdot 0.73}{1.004 \cdot 10^{-6}} \approx 10^6 \quad (38)$$

Intuitively, this value brings the laminar-turbulent flow transition region into question for evaluating coefficient of drag parameters, since this lies above the typical critical Reynolds number of $\approx 5 \cdot 10^5$ for a sphere or cylinder in cross flow (See Figs. 11 and 12 in [16]). However, since shorter, individual pieces are being evaluated for drag, and flow in all directions is not expected to be as high as the very top speed for LoCO, the drag parameters for the vehicle are assumed to be in the subcritical Reynolds number region.

First, the individual coefficients of drag must be found for each component. Hoerner [16] is used to provide approximations for all the geometric shapes used, and figures referenced below are from the same text. As mentioned in the previous section, the length to diameter ratio for the long tubes is approximately 5, and for the thruster approximations is about 0.5. Hoerner Figure 3-21 for axial flow across cylindrical bodies can be used to approximate the total coefficients of drag for these two shapes in axial flow. This total drag coefficient given includes skin friction effects. This provides an axial drag coefficient of about 0.8258 for the tubes using the blunt nose line. Though the thrusters are approximated in shape as blunt cylinders, they do have a short, rounded portion on either side. In an attempt to account for this, the average of the blunt nose and streamlined head forms is taken and provides a total axial drag coefficient of approximately 0.75 for the thrusters. For flow across these same cylinders normal to their center axis, Hoerner Figure 3-12 for the drag coefficient of a circular cylinder in the same flow conditions can be used where the 1.2 approximation just before the transition point is used. Since there is relatively low surface area, skin friction effects are neglected.

The sectional drag coefficient values for the rectangular prisms can be obtained using Hoerner Figures 3-22 and 3-23. For axial flow with all rectangular prisms, the

length to thickness ratio is approximately or above 2.5. So, from Hoerner Figure 3-22, the total drag coefficient in axial flow is approximately 1 and includes skin friction effects. In cross flow, the 3D-printed parts have a slight radius on the edges. This ratio of radius to width of the cross section is about 0.1, so the sectional drag coefficient is approximately 2. Again, as these are bluff bodies in cross flow, the skin friction is considered negligible. A summary of these drag coefficients are given in Table 5 below.

Component	Axial Total C_D	Cross Flow Total C_D
Tube	0.8258	1.2
Thruster	0.75	1.2
Long Backbone	1	Not Needed
Any Square Rectangular Prism (“rect”)	Not Needed	2

Table 5: Summary of component coefficients of drag.

Another useful table to express parameters used in determining drag are the reference areas applicable to the coefficients of drag used in Table 5. Using the component geometries listed in Table 6,

Component	$A_{ref_{axial}}$ (m^2)	Cross Flow $A_{ref_{cross}}$ (m^2)
Tube	0.010136	0.06109
Thruster	0.007322	0.004291
Long Backbone	0.0017564	Not Needed
Clamp Connectors	Not Needed	0.004287
Connector Side Block	Not Needed	0.0012655
Strut Side Block	Not Needed	0.0016500
Long Backbone	Not Needed	0.006094
Rear Strut	Not Needed	0.005056

Table 6: Summary of component drag reference areas.

Beginning with the equation for linear drag in the x direction with the X-Model,

$$\begin{aligned}
X_{u|u} = & -\frac{1}{2} \rho (2 \cdot C_{D_{axial_{tube}}} \cdot Aref_{axial_{tube}} + 2 \cdot C_{D_{axial_{thruster}}} \cdot Aref_{axial_{thruster}} \dots \\
& + C_{D_{cross_{thruster}}} \cdot Aref_{cross_{thruster}} + C_{D_{axial_{long_back}}} \cdot Aref_{axial_{long_back}} \dots \\
& + 2 \cdot C_{D_{cross_{rect}}} \cdot Aref_{cross_{connector_side}} \dots \\
& + 2 \cdot C_{D_{cross_{rect}}} \cdot Aref_{cross_{strut_side}}) \quad (39)
\end{aligned}$$

Due to symmetry, drag caused by motion in the x direction does not also cause a net yaw moment on the model. Then for the lateral direction with the Y-Model,

$$\begin{aligned}
Y_{v|v} = & -\frac{1}{2} \rho (2 \cdot C_{D_{cross_{tube}}} \cdot Aref_{cross_{tube}} + 2 \cdot C_{D_{cross_{thruster}}} \cdot Aref_{cross_{thruster}} \dots \\
& + C_{D_{cross_{backbone}}} \cdot Aref_{cross_{backbone}}) \quad (40)
\end{aligned}$$

With this, there is also a net yaw drag moment caused by linear motion in the y direction. With each coefficient tied to a force in the y direction, the coefficient for each component can be multiplied by its center offset in the x direction causing rotation about the yaw axis,

$$\begin{aligned}
N_{v|v} = & \frac{1}{2} \rho (-2 \cdot C_{D_{cross_{tube}}} \cdot Aref_{cross_{tube}} \cdot x_{C_{tube}} \dots \\
& + 2 \cdot C_{D_{cross_{thruster}}} \cdot Aref_{cross_{thruster}} \cdot x_{C_{rear_thruster}} \dots \\
& + C_{D_{cross_{backbone}}} \cdot Aref_{cross_{backbone}} \cdot x_{C_{backbone}}) \quad (41)
\end{aligned}$$

And finally in the vertical direction using the Z-Model,

$$\begin{aligned}
Z_{w|w} = & -\frac{1}{2} \rho (2 \cdot C_{D_{cross_{tube}}} \cdot Aref_{cross_{tube}} + C_{D_{axial_{thruster}}} \cdot Aref_{axial_{thruster}} \dots \\
& + 2 \cdot C_{D_{cross_{thruster}}} \cdot Aref_{cross_{thruster}} + C_{D_{cross_{backbone}}} \cdot Aref_{cross_{backbone}} \dots \\
& + 2 \cdot C_{D_{cross_{connector}}} \cdot Aref_{cross_{connector}} \dots \\
& + C_{D_{cross_{strut}}} \cdot Aref_{cross_{strut}}) \quad (42)
\end{aligned}$$

There is also a net pitch drag moment caused by linear motion in the z direction. With each coefficient tied to a force in the z direction, the coefficient for each component can be multiplied by its center offset in the x direction causing rotation about the pitch axis,

$$\begin{aligned}
M_{w|w|} = & \frac{1}{2} \rho (2 \cdot C_{D_{cross\ tube}} \cdot A_{ref_{cross\ tube}} \cdot xC_{tube} \dots \\
& + C_{D_{axial\ thruster}} \cdot A_{ref_{axial\ thruster}} \cdot xC_{fore_thruster} \dots \\
& + 2 \cdot C_{D_{cross\ thruster}} \cdot A_{ref_{cross\ thruster}} \cdot xC_{rear_thruster} \dots \\
& + C_{D_{cross\ backbone}} \cdot A_{ref_{cross\ backbone}} \cdot xC_{backbone} \dots \\
& + 2 \cdot C_{D_{cross\ connector}} \cdot A_{ref_{cross\ connector}} \cdot xC_{connector} \dots \\
& + C_{D_{cross\ strut}} \cdot A_{ref_{cross\ strut}} \cdot xC_{strut}) \quad (43)
\end{aligned}$$

Now the moment damping coefficients must be determined. For roll damping, the Z-Model can be used. The damping with the rotation of the backbone and vertical thruster through their center axes may be neglected. For the tubes and rear thrusters, a roll motion can be approximated as instantaneously vertical motion at a distance away from the roll axis. Rather than the typical integral expression in equation 16 that will be used for the clamp connectors and the rear strut, this moment damping can be expressed as

$$M_D = F_D \perp r = -\frac{1}{2} \rho C_D (R_n) A_{ref} |\omega| \omega \cdot r^2 |r| \quad (44)$$

where r is the perpendicular distance from the axis of rotation. Expressing the roll damping coefficient,

$$\begin{aligned}
K_{p|p|} = & -\frac{1}{2} \rho (2 \cdot C_{D_{cross\ tube}} \cdot A_{ref_{cross\ tube}} \cdot yC_{tube}^3 \dots \\
& + 2 \cdot C_{D_{cross\ thruster}} \cdot A_{ref_{cross\ thruster}} \cdot yC_{rear_thruster}^3 \dots
\end{aligned}$$

$$\begin{aligned}
& + C_{D_{cross_connector}} \cdot width_{connector} \cdot \frac{(length_{connector}/2)^4}{4} \dots \\
& + C_{D_{cross_strut}} \cdot width_{strut} \cdot \frac{(length_{strut}/2)^4}{4} \dots
\end{aligned} \tag{45}$$

Next is the pitch damping coefficient for the underwater vehicle using the Z-Model. In this motion, the moments for the tubes, rear thrusters, and backbone must be integrated as in equation 16, but the remaining components utilize the modified equation 44.

$$\begin{aligned}
M_{q|q} = & -\frac{1}{2} \rho \cdot \left(2 \cdot C_{D_{cross_tube}} \cdot width_{tube} \cdot \frac{(x2_{tube}^3 |x2_{tube}| - x1_{tube}^3 |x1_{tube}|)}{4} \right) \dots \\
& + \left(2 \cdot C_{D_{cross_thruster}} \cdot H_{thruster} \cdot \frac{(x2_{rear_thruster}^3 |x2_{rear_thruster}| - x1_{rear_thruster}^3 |x1_{rear_thruster}|)}{4} \right) \dots \\
& + \left(C_{D_{cross_backbone}} \cdot length_{backbone} \cdot \frac{(x2_{backbone}^3 |x2_{backbone}| - x1_{backbone}^3 |x1_{backbone}|)}{4} \right) \dots \\
& + (C_{D_{axial_thruster}} \cdot Aref_{axial_thruster} \cdot xc_{fore_thruster}^3) \dots \\
& + (C_{D_{cross_connector}} \cdot Aref_{cross_connector} \cdot xc_{fore_connector}^3) \dots \\
& + (C_{D_{cross_connector}} \cdot Aref_{cross_connector} \cdot xc_{aft_connector}^3) \dots \\
& + (C_{D_{cross_strut}} \cdot Aref_{cross_strut} \cdot |xc_{strut}^3|)
\end{aligned} \tag{46}$$

Finally for the yaw damping coefficient using the Y-Model, all components must be integrated using equation 16. As explained with the yaw added mass, it is assumed that yaw motion produces an instantaneous velocity in the y direction, so component offsets in the x direction cancel and are not considered.

$$\begin{aligned}
N_{r|r} = & -\frac{1}{2} \rho \cdot \left(2 \cdot C_{D_{cross\ tube}} \cdot H_{tube} \cdot \frac{(x_{2\ tube}^3 |x_{2\ tube}| - x_{1\ tube}^3 |x_{1\ tube}|)}{4} \right) \dots \\
& + \left(2 \cdot C_{D_{cross\ thruster}} \cdot H_{thruster} \cdot \frac{(x_{2\ rear\ thruster}^3 |x_{2\ rear\ thruster}| - x_{1\ rear\ thruster}^3 |x_{1\ rear\ thruster}|)}{4} \right) \dots \\
& + \left(C_{D_{cross\ backbone}} \cdot length_{backbone} \cdot \frac{(x_{2\ backbone}^3 |x_{2\ backbone}| - x_{1\ backbone}^3 |x_{1\ backbone}|)}{4} \right) \quad (47)
\end{aligned}$$

Evaluating all equations for determining the damping coefficients, the results of the computations are given below in Table 7.

Parameter Description	Variable	Value	Units
Water Density	ρ	1000	kg/m ³
Hydrodynamic Damping Coefficients	$X_{u u}$	-23.14	kg/m
	$Y_{v v}$	-84.56	kg/m
	$Z_{w w}$	-100.93	kg/m
	$K_{p p}$	-0.09952	kg m ²
	$M_{q q}$	-3.237	kg m ²
	$N_{r r}$	-2.831	kg m ²
	$M_{w w}$	20.55	kg
	$N_{v v}$	-18.60	kg

Table 7: Summary of hydrodynamic damping analysis results.

3.6. Dynamic Equations for LoCO

Among the various parameters derived and discussed in this section, a table of final values to be inserted into final dynamic equations, including some extra geometric terms for the propulsion system, is shown below based on the analyses and simplifying assumptions in each section. For the purpose of clarity, the actual values will not be inserted and displayed.

Parameter Description	Variable	Value	Units
Water Density	ρ	1000	kg/m ³
Buoyancy Force	B	123.02	N
Center of Buoyancy	CB _x	0.2417	m
	CB _y	0	m
	CB _z	0	m

Mass	m	12.545	kg
Weight	W	123.02	N
Center of Gravity	CG _x	0.2417	m
	CG _y	0	m
	CG _z	0	m
Moments of Inertia	I _x	0.19094	kg m ²
	I _y	1.2050	kg m ²
	I _z	1.3465	kg m ²
	I _{xy}	0	kg m ²
	I _{yz}	0	kg m ²
	I _{xz}	0	kg m ²
Added Mass	X _ü	2.899	kg
	Y _{v̇}	11.855	kg
	Z _{ẇ}	12.915	kg
	K _{ṗ}	0.13557	kg m ²
	M _{q̇}	1.4260	kg m ²
	N _{ṙ}	1.0667	kg m ²
	Z _{q̇}	-3.562	kg m
	M _{ẇ}	-3.562	kg m
	Y _{ṙ}	2.818	kg m
	N _{v̇}	2.818	kg m
Hydrodynamic Damping Coefficients	X _{u u}	-23.14	kg/m
	Y _{v v}	-84.56	kg/m
	Z _{w w}	-100.93	kg/m
	K _{p p}	-0.09952	kg m ²
	M _{q q}	-3.237	kg m ²
	N _{r r}	-2.831	kg m ²
	M _{w w}	20.55	kg
	N _{v v}	-18.60	kg
Relevant Thruster Offsets	x _{Cfore}	0.4156	m
	y _{Cport}	-0.10932	m
	y _{Cstarboard}	0.10932	m

Table 8: Relevant dynamic model parameters from analysis and estimation.

Expressing the final dynamic equations for LoCO,

Surge

$$\begin{aligned}
m(\dot{u} - vr + wq - x_G(q^2 + r^2)) &= T_{port} + T_{stbd} + X_{u|u|}u|u| \dots \\
&\quad - (X_{\dot{u}}\dot{u} + Z_{\dot{w}}wq + Z_{\dot{q}}q^2 - Y_{\dot{v}}vr - Y_{\dot{r}}r^2)
\end{aligned} \tag{48a}$$

Sway

$$\begin{aligned} m(\dot{v} - wp + ur + x_G(qp + \dot{r})) &= Y_{v|v}|v|v| \dots \\ &- (Y_{\dot{v}}\dot{v} + Y_{\dot{r}}\dot{r} + X_{\dot{u}}ur - Z_{\dot{w}}wp - Z_{\dot{q}}pq) \end{aligned} \quad (48b)$$

Heave

$$\begin{aligned} m(\dot{w} - uq + vp + x_G(rp - \dot{q})) &= T_{fore} + Z_{w|w}|w|w| \dots \\ &- (Z_{\dot{w}}\dot{w} + Z_{\dot{q}}\dot{q} - X_{\dot{u}}uq + Y_{\dot{v}}vp + Y_{\dot{r}}rp) \end{aligned} \quad (48c)$$

Roll

$$\begin{aligned} I_x\dot{p} + (I_z - I_y)qr &= K_{p|p}|p|p| \dots \\ - (K_{\dot{p}}\dot{p} - (Y_{\dot{v}} - Z_{\dot{w}})vw - (Y_{\dot{r}} + Z_{\dot{q}})wr + (Y_{\dot{r}} + Z_{\dot{q}})vq - (M_{\dot{q}} - N_{\dot{r}})qr) \end{aligned} \quad (48d)$$

Pitch

$$\begin{aligned} I_y\dot{q} + (I_x - I_z)rp + m(-x_G(\dot{w} - uq + vp)) &= -T_{fore} x_{c_{fore}} \dots \\ + M_{q|q}|q|q| + M_{w|w}|w|w| - (Z_{\dot{q}}(\dot{w} - uq) + M_{\dot{q}}\dot{q} - (Z_{\dot{w}} - X_{\dot{u}})wu) &\dots \\ - Y_{\dot{r}}vp + (K_{\dot{p}} - N_{\dot{r}})rp \end{aligned} \quad (48e)$$

Yaw

$$\begin{aligned} I_z\dot{r} + (I_y - I_x)pq + m(x_G(\dot{v} - wp + ur)) &= -T_{port} y_{c_{port}} - T_{stbd} y_{c_{stbd}} \dots \\ + N_{r|r}|r|r| + N_{v|v}|v|v| - (Y_{\dot{r}}\dot{v} + N_{\dot{r}}\dot{r} - (X_{\dot{u}} - Y_{\dot{v}})uv + Y_{\dot{r}}ur + Z_{\dot{q}}wp) &\dots \\ - (K_{\dot{p}} - M_{\dot{q}})pq \end{aligned} \quad (48f)$$

3.7. Conclusion

In this chapter, the various physical and hydrodynamic values for LoCO have been determined. Parameters relating to buoyancy were determined using analytical methods and the CAD model of LoCO. Mass and moment of inertia values were also

obtained using the CAD model of LoCO along with computational estimation, analytical methods, and physical measurements. General assumptions have been made for each of these cases in order to simplify the governing dynamic models of the underwater vehicle. The more complex geometry of LoCO was simplified into three different geometric models that attempt to approximate added mass and hydrodynamic damping measures based on a composite makeup of simpler shapes. Final parametrized dynamic equations for LoCO are presented that allow the next step in simulating the AUV.

Chapter 4

Simulation

4.1. Introduction

There are a number of different simulation software programs that can be used in a dynamic simulation of a rigid body, such as Matlab or Unreal Engine. However, a simulation program that is able to directly interface with LoCO's software and Robot Operating System (ROS) framework is Gazebo [25]. Like ROS, Gazebo is an open-source platform for robotics and other software development that enables the visualization and physics simulation of robots without requiring real-world testing. This is especially valuable in the field of underwater robotics with a relatively unforgiving environment in the case of equipment failures.

4.2. Modeling and Visualization

The modeling and visualization of LoCO in the simulation software is based on the SolidWorks CAD design model as seen earlier in the thesis. It is used as the template for creating the Universal Robotic Description Format (URDF) file for the robot, which is an XML-based file format for representing the model of a robot. Components of the robot are connected to the main robot frame or other components through "links", like the linkages of a robot arm. The inertial matrix for LoCO is based on the estimates made in Chapter 3, along with its mass. In order to improve the efficiency of the simulation without affecting the physics engine, the mesh file generated by SolidWorks to provide the visual representation of LoCO does not include internal components. This physical

model for LoCO in a basic simulated world can be seen in Fig. 13. There are, however, some components modeled independent of the mesh. The black boxes near the front of the AUV represent the cameras that allow for the use of the vision systems in simulation. The green propeller blades, otherwise known as the thruster links, are also included to allow for the modeling of LoCO's motion. The inertial and mass properties for the individual cameras and thruster propellers are assumed negligible. However, as Gazebo will not recognize links with exactly zero inertial or mass value, all negligible values for cameras and propellers were given on the order of $1e-5$.

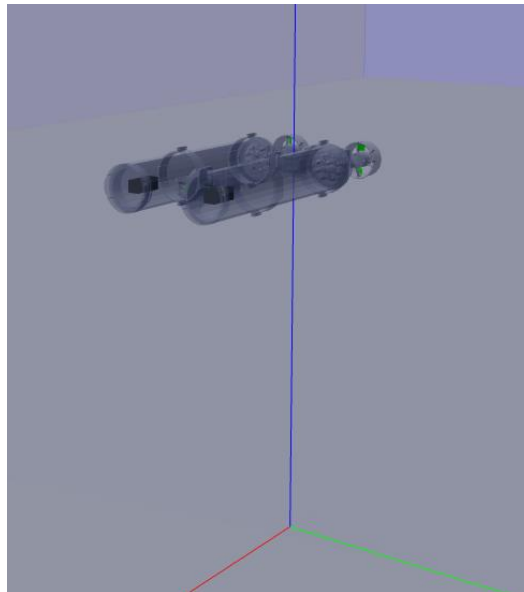


Figure 13: LoCO in a simulated Gazebo world.

In Gazebo, there are collision properties associated with each link or component of the robot so the simulation can model the physical impacts between the robot and its surroundings. The collision geometric boundaries are modeled to be the same as all of the visual boundaries for each link except for the main body of LoCO. Due to the complexity and size of the mesh, even at its relatively coarse mesh size, the collision boundary for

the main body is modeled as a box so as to lower the computational requirements of the simulation. The GazeboRosControl plugin is also incorporated in the URDF file to load appropriate hardware interfaces, control managers, and transmission tags into Gazebo for simulation.

4.3. Physics

The physics engine implemented in Gazebo is the Open Dynamics Engine (ODE) [26]. Fluid mechanics and other real-world forces are not directly simulated in Gazebo. Instead, the hydrodynamic forces must be calculated within a ROS node then applied to the underwater vehicle model. First, in general, the ODE physics engine automatically applies a standard gravitational force to the model. With LoCO neutrally buoyant, a Gazebo plugin called “BuoyancyPlugin” applies the appropriate buoyancy force based on the specified water density and volume of the model. Although the displacement volume of LoCO has already been estimated, a volume made to match the collision bounding box is set in the model to achieve neutral buoyancy.

There are a number of ways to simulate LoCO’s propeller propulsion. For example, there is the Gazebo LiftDragPlugin that computes the thrust generated by spinning airfoils of given properties, or there are direct ROS Twist messages that can be sent to the simulation that directly control the velocity of the thrusters. However, with the established assumption that the thrusters provide point forces, the GazeboRosForce plugin was implemented to directly apply thruster forces to each of the thrusters. The simple physical models for the propellers have been left in the simulation in the case of future propeller dynamics integration. The underwater thrust force data for the T100

thruster from Blue Robotics is readily available on their website and discussed further in Chapter 5.

However, issues with ROS communication arose with this approach. Messages sent to the simulation to apply forces to the thrusters are only sent one at a time. Theoretically, the messages are all sent simultaneously, but even with only slight computation delay, certain LoCO motions cause a buildup in robot movement error. So, it was determined that all forces and moments on the robot would be summed and applied to vehicle frame origin through the same GazeboRosForce plugin as described in Chapter 3.

4.4. Simulation Architecture and Control

This ROS node graph in Fig. 14 shows the main working parts of the simulation, but the three critical aspects are the teleop keyboard program on the left, the sim control node program in the middle, and the Gazebo simulation on the right. The teleop keyboard is a program that sends the simulated robot thruster commands based on keyboard input. The Gazebo component on the far right is the actual simulation, where force commands and physics are applied to the robot. The sim control node highlighted in red is what bridges existing LoCO software with the simulation. It reads in the commands from the teleop node, reads in the state of the robot from Gazebo, then performs the necessary rotations to the force vectors and applies these to the simulation model.

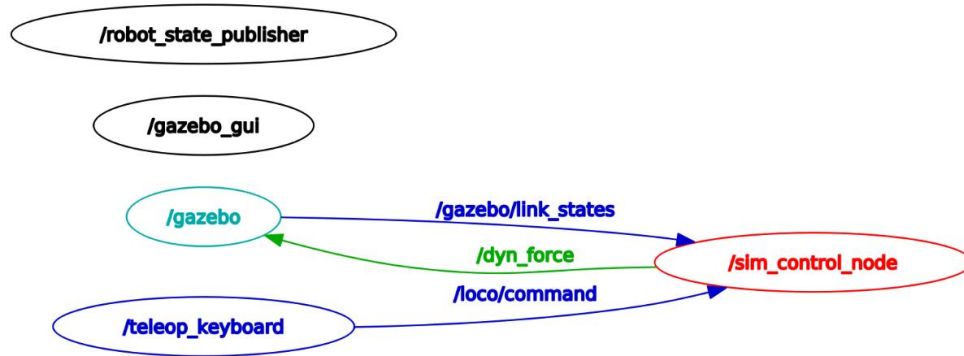


Figure 14: ROS program nodes and messages used to run the simulation.

4.5. Quaternions and Force Application

Due to the possible shortcomings with singularities of using Euler angles to determine the robot coordinate frame orientation, and to reduce computation requirements, quaternions are used in the simulation instead. Quaternions are a mathematical representation of a four-dimensional framework defined as

$$\mathbf{q} = q_0 + q_1 \mathbf{i} + q_2 \mathbf{j} + q_3 \mathbf{k} \quad (49)$$

where q_0 is a real number, and unit vectors \mathbf{i} , \mathbf{j} , \mathbf{k} , are imaginary unit vectors expressing an imaginary dimension. One of the primary practical uses with quaternions comes with 3D rotations, and when $q_0=0$, the remaining elements come to represent the typical 3 dimensions in space. For example, a quaternion where $q_1=1$ and all other components equal 0 represents a unit vector in the x direction. More on the details of quaternions and their mathematical properties can be found in sources such as [27].

During a simulation, Gazebo keeps track of the quaternion representation of the orientation of a robot. However, the GazeboRosForce plugin is only able to apply forces and in the global coordinate frame, so the desired force and moment vectors must be

rotated. Each time the simulation runs through the simulation control node, that quaternion frame representation is received from Gazebo. To achieve the rotation of a vector into the coordinate system represented by a quaternion, the following equation can be used,

$$\mathbf{v}_{body_frame} = (\mathbf{q} \cdot \mathbf{v}) \cdot \mathbf{q}^* \quad (50)$$

where \mathbf{v} is the original vector in three-dimensional space represented as a quaternion where q_0 appropriately is set to 0, \mathbf{q}^* is the conjugate of the quaternion \mathbf{q} , and all multiplication performed is quaternion multiplication. In the simulation, this multiplication is done with each inertial x, y, and z direction unit vector to determine the new unit vector representation of each body axis.

Also, Gazebo also only registers the actual velocities of the vehicle in the global coordinate frame, so dot products are performed appropriately to find the velocities and accelerations in the relative body frame. Once this is done, the sum of the forces and moments are calculated as depicted at the end of Chapter 3. The final computation requires additional dot products to translate relative forces and moments back into forces applied in the global coordinate frame. This method also accounts for the fact that the inertial axis in Gazebo is oriented differently than the body axes for which the equations of motion are derived, as can be seen in Fig. 13.

4.6. Conclusion

In this chapter, an overview of the Gazebo-based simulation for LoCO has been given. The physical modeling aspects of LoCO come from the CAD model and estimates made in the previous chapter, and the physics for the simulation has been discussed. The

basic control framework for the simulation is based on ROS nodes and is made to allow an interface between existing LoCO software and the simulation world. Finally, quaternion rotations are used to correctly apply forces to the robot model for computational efficiency and regardless of the model state.

Chapter 5

Experimental Data and Comparison with Simulation

5.1. Introduction

Though analytical modeling and simulations can be performed to approximate the dynamic properties of a vehicle, real world testing is still critical. For full scale ships, dynamic characterization is often performed on a scale model in a tow tank that can maintain a given set of motions. The experimental testing with LoCO, however, occurred within a pool setting during a regular trial period. The currently available motion set of data is for straight line, horizontal motion at various thruster throttle commands.

5.2. Experiment and Data Analysis

Since the forward motion of an underwater vehicle is arguably the most critical and simplest motion to test, this serves as the starting point for experimental data. Inertial measurement unit (IMU) data was collected at various equal rear thruster forces to provide a range of steady state velocities for LoCO. Each test case was repeated and averaged in order to confirm results.

The test cases for the experiment were based on throttle command, or a proportion of the maximum pulse width modulator (PWM) input to the electronic speed controller. The published thrust data for the T100 Blue Robotics thrusters can be seen below in Fig. 15 [28]. Throttle commands range from -1 to 1, with a command of 0 centered at an input of 1500 μ s. For example, a throttle command of 0.5 translates to 1700 μ s. This

relationship was used to translate throttle command data into an axial force exerted by the thrusters on the robot.

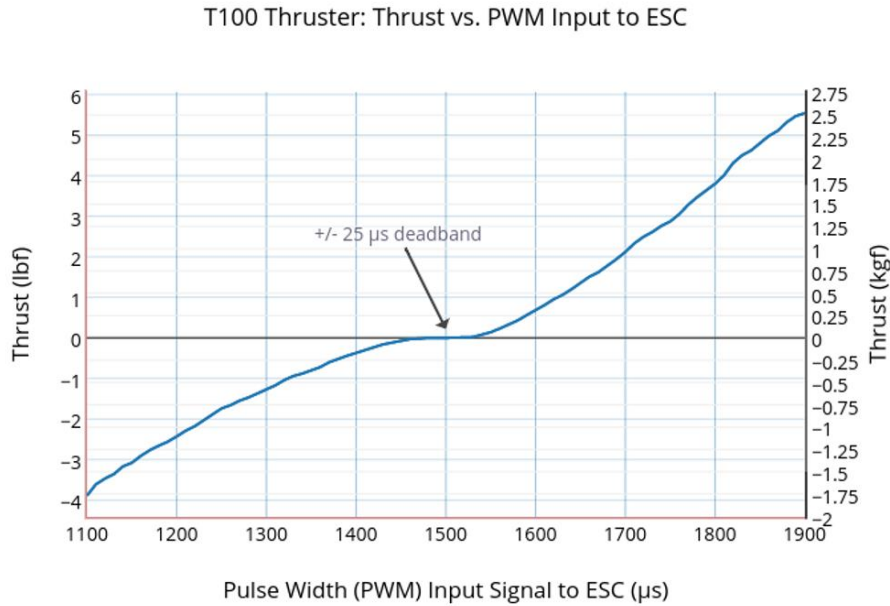


Figure 15: Thruster force versus PWM input [28].

IMU data was logged with the Pixhawk through the Mavros ROS package. Though tests were designed to be straight and horizontal, there was inevitably some variability in the robot motion, primarily a slight net pitching moment due to water seeping into some of the rear 3D printed components at the time. Conveniently, the Mavros package also provides the quaternion coordinate frame state of the robot on top of the acceleration data. So, like the frame rotations described in Section 4.5, any effect of the acceleration due to gravity on acceleration in the relative forward direction of the robot is filtered out. Maximum forward velocity for each throttle case was determined through trapezoidal integration of IMU acceleration data from the test start through the

point where steady state was reached. The results of this data analysis are shown in the following section.

5.3. Simulation Data Comparison

With experimental data gathered for the forward motion case, the simulation can be compared to real data. Tests equivalent to the ones performed in the pool were performed in simulation for horizontal, straight line LoCO motion.

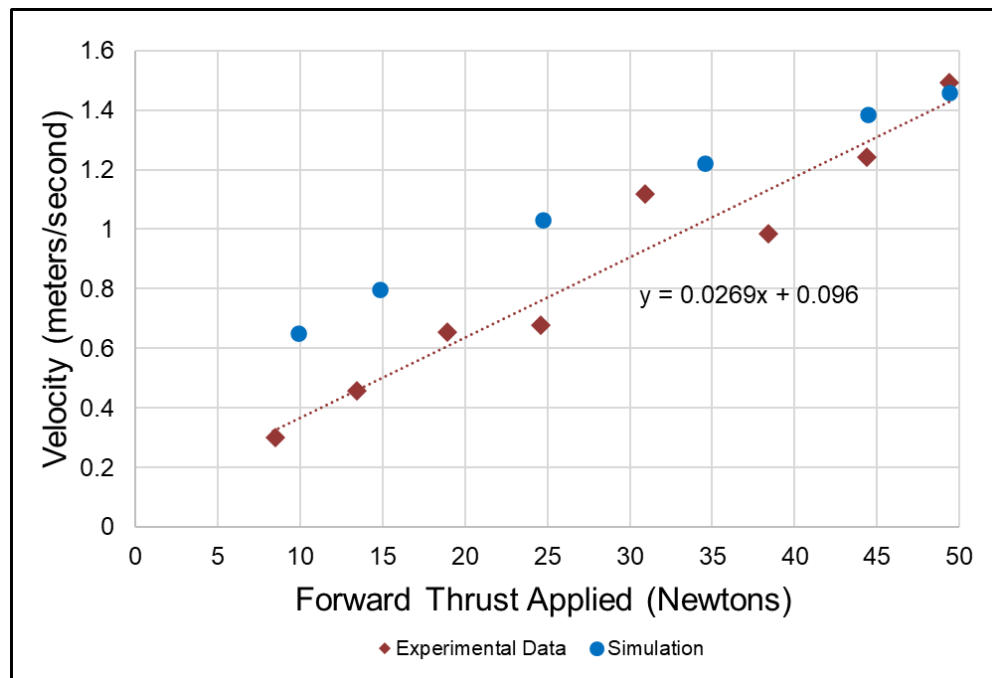


Figure 16: Velocity versus forward thrust applied for a straight line, horizontal path in a pool.

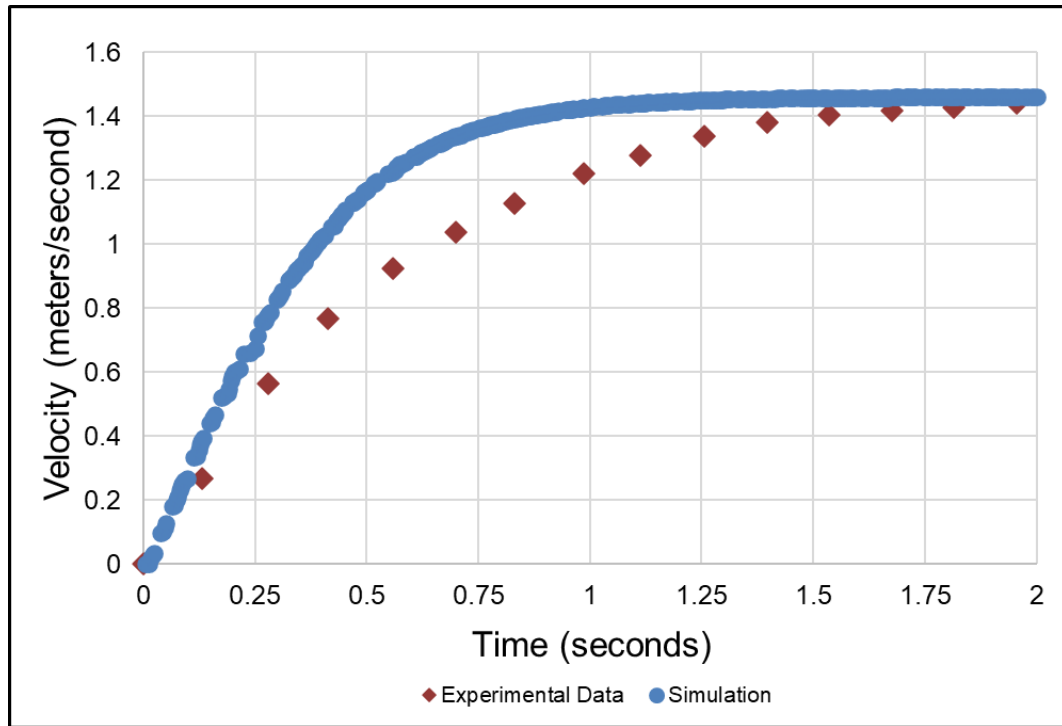


Figure 17: Velocity versus full forward thrust applied for a straight line, horizontal path.

Though drag is characteristically a function of the square of velocity, results from the experimental testing display a linear trend, likely due to the data’s overall proximity to “1” meter per second. It can be seen from Fig. 16 that the simulation tends to overpredict the velocity achievable by the vehicle at lower thrust but converges to the experimental data at the highest thrust of approximately 50 N. One possibility for this discrepancy is some additional skin friction or viscous drag more prevalent at lower velocities than predicted by simulation. Then, at higher velocities, this drag returns to being relatively negligible as predicted by the simulation.

Fig. 17 is included to examine the velocity profile for LoCO as it approaches its top speed of approximately 1.5 meters per second. Though as expected from the first graph, the steady state velocities can be considered the same, the simulation acceleration

is higher than the experimental data. Part of this may be due to the higher drag than expected at lower velocities as seen in the Fig. 15. Another possibility is that the added mass estimates made from Equation 28 resulting from computational fluid dynamics simulations in [23] could tend to be lower than actual results. A higher added mass would also effectively decrease the acceleration of the vehicle and bring the simulation curve down to the experimental data.

Since experimental data was only gathered for surge motion, comparisons are not able to be made between the dynamic model and real-world data for other motions, such as yaw or pitching in the vertical plane. Further analysis and testing are required to verify the presented dynamic modeling for LoCO.

5.4. Conclusion

Experimental trials have been run for LoCO's motion in horizontal, straight paths. Forward acceleration relative to the vehicle was isolated during analysis by filtering data with quaternion rotation. This testing has established a maximum speed of approximately 1.5 meters per second and provided overall estimates on forward velocity profiles. Simulation data for the same type of motion has been gathered and compared to the experimental results. Though the maximum velocity for LoCO in simulation correlates well to real data, the simulation typically leads to higher predicted velocities at lower thrusts than seen in experiments. This leads to suspected drag forces at lower velocities not currently accounted for in the simulation. Further testing is required in order to validate the dynamic modeling for other LoCO motions, such as pitch and yaw.

Chapter 6

Conclusion

6.1. Review

In this thesis, the dynamic modeling and simulation of the LoCO AUV has been presented. An introduction to LoCO is given, following by the establishment of a foundation for dynamic derivations. The equations of motion for LoCO in 6 DOF are derived, and the corresponding forces are brought to attention in Chapter 2. The following chapter goes on to evaluate the presented coefficients and constants associated with the geometry of LoCO. The resulting finalized dynamic equations are implemented in a Gazebo-based simulator that is able to interface with onboard robot software. Chapter 5 presents the testing performed to obtain experimental surge data for LoCO's motion. An overview of the data analysis is given and compared to equivalent simulation experiment data.

6.2. Conclusions

Overall, this thesis sought to derive the dynamic equations for an underwater vehicle such as LoCO and evaluate the geometric-dependent parameters using established assumptions. Further, the model was to be implemented in a simulation and compared with experimental data obtained in a pool trial. The thesis has been primarily successful in all these points, but more analysis and real-world testing is required to firmly validate the full dynamic model for the vehicle.

6.3. Future Work

From this work, the foundation for dynamic characterization of the vehicle is established. Autonomous behavior and control system development can use the developed models to improve LoCO's ability to perform underwater operations and assist personnel. Also, the dynamic models have been derived with respect to the rear of the tubes on the robot, rather than the center of gravity, which can certainly change as the robot development is continued. This allows for the easiest possible future modification of the dynamic models presented herein as the robot changes and additional equipment or sensors are implemented.

References

- [1] A. B. Rechnitzer and J. D. Baker, “Undersea exploration,” *Encyclopedia Britannica*. 2017.
- [2] M. Sahi, “Challenges for Underwater Robotics,” 2015. [Online]. Available: <https://www.tractica.com/automation-robotics/challenges-for-underwater-robots/>. [Accessed: 12-Oct-2019].
- [3] C. C. Eriksen *et al.*, “Seaglider : A Long-Range Autonomous Underwater Vehicle for Oceanographic Research,” *IEEE J. Ocean. Eng.*, vol. 26, no. 4, pp. 424–436, 2001.
- [4] C. Edge *et al.*, “Design and experiments with LoCO AUV: A low cost open-source autonomous underwater vehicle,” *IEEE Int. Conf. Intell. Robot. Syst.*, pp. 1761–1768, 2020.
- [5] S. Heshmati-alamdari, “Cooperative and Interaction Control for Underwater Robotic Vehicles,” National Technical University of Athens, 2018.
- [6] T. Prestero, “Verification of a Six-Degree of Freedom Simulation Model for the REMUS Autonomous Underwater Vehicle,” Massachusetts Institute of Technology, Woods Hole Oceanographic Institution, 2001.
- [7] M. Fulton, M. Ahmed, and J. Sattar, “By Land, Air, or Sea: Multi-Domain Robot Communication Via Motion,” no. March, 2019.
- [8] C. Hajiyev, “Autonomous Vehicles: Intelligent Transport Systems and Smart Technologies,” 2014, pp. 81–111.
- [9] G. D. Watt, “Deeply Submerged Hydrodynamic , Control , Propulsion , and

- Dynamic Change Models for Underwater Vehicle Simulation,” no. November, 2019.
- [10] T. Fossen, *Handbook of Marine Craft Hydrodynamics and Motion Control*. John Wiley & Sons Ltd, 2011.
- [11] J. Peraire, “Lecture L29 - 3D Rigid-Body Dynamics.” Massachusetts Institute of Technology: MIT OpenCourseWare, 2009.
- [12] H. A. Ardakani and T. J. Bridges, “Review of the 3-2-1 Euler Angles : a yaw – pitch – roll sequence,” pp. 1–9, 2010.
- [13] A. Techet, “2.016 Hydrodynamics.” Massachusetts Institute of Technology: MIT OpenCourseWare, 2005.
- [14] SNAME The Society of Naval Architects and Marine Engineers, “Nomenclature for Treating the Motion of a Submerged Body Through a Fluid,” *Technical and Research Bulletin*, vol. 1–5. 1950.
- [15] F. Imlay, “The complete expressions for added mass of a rigid body moving in an ideal fluid,” 1961.
- [16] S. Hoerner, *Fluid-Dynamic Drag*. Sighard Hoerner, 1965.
- [17] S. C. Tang, “Modeling and Simulation of the Autonomous Underwater Vehicle, Autolytus,” MASSACHUSETTS INSTITUTE OF TECHNOLOGY, 1999.
- [18] American National Standard, “Medium Density Fiberboard (MDF) For Interior Applications.” American National Standard, 2002.
- [19] MatWeb, “Aluminum 6061-T6; 6061-T651,” 2021. [Online]. Available: <http://www.matweb.com/search/DataSheet.aspx?MatGUID=b8d536e0b9b54bd7b69e4124d8f1d20a&ckck=1>.

- [20] The_University_of_Tennessee, “4-3: Mass Moment of Inertia.” [Online]. Available: <https://efcms.engr.utk.edu/ef151-2019-08/sys.php?f=bolt/bolt-main&c=class-4-3&p=mmi>.
- [21] M. I. of T. M. OpenCourseWare, “2.20 - Marine Hydrodynamics Lecture 13.” Massachusetts Institute of Technology: MIT OpenCourseWare, 2005.
- [22] E. V Lewis, *Principles of Naval Architecture Second Revision Volume III Motions in Waves and Controllability*, vol. 3. 1989.
- [23] M. Elgabaili, “HYDRODYNAMIC MASS OF BLUFF BODIES WITH AND WITHOUT CAVITY,” CALIFORNIA STATE UNIVERSITY, NORTHRIDGE, 2012.
- [24] E. Edge, “Water - Density Viscosity Specific Weight,” 2021. [Online]. Available: https://www.engineersedge.com/physics/water__density_viscosity_specific_weight_13146.htm.
- [25] Open_Source_Robotics_Foundation, “Gazebo,” 2014. [Online]. Available: <http://gazebosim.org/>.
- [26] R. Smith, “Open Dynamics Engine,” 2004. [Online]. Available: <https://www.ode.org/>.
- [27] E. Weisstein, “Quaternion,” *Wolfram MathWorld*, 2021. [Online]. Available: <https://mathworld.wolfram.com/Quaternion.html>.
- [28] B. Robotics, “T100 Thruster,” 2015. [Online]. Available: <https://bluerobotics.com/store/retired/t100-thruster/>.

Appendix A

Description	Mass (kg)	CG X Displacement (m)	CG Y Displacement (m)	CG Z Displacement (m)	Local Moment of Inertia per kg (*If Derived Analytically)						
					Ixx	Iyy	Izz	Ixy	Iyz	Ixz	
Left Tube											
Left Battery*	0.5650	0.3242	-0.1205	-0.0114	0.0004	0.0028	0.0025	0.0000	0.0000	0.0000	
Right Battery*	0.5650	0.3242	-0.0955	-0.0114	0.0004	0.0028	0.0025	0.0000	0.0000	0.0000	
Polycarbonate Tube*	2.0412	0.2660	-0.1080	0.0000	0.0029	0.0230	0.0230	0.0000	0.0000	0.0000	
Front End Cap	0.1590	0.4752	-0.1080	0.0000	0.0017	0.0008	0.0009	0.0000	0.0000	0.0000	
Front Flange Seal	0.1440	0.5150	-0.1080	0.0000	0.0024	0.0013	0.0013	0.0000	0.0000	0.0000	
Rear Flange Seal	0.1440	0.0170	-0.1080	0.0000	0.0024	0.0013	0.0013	0.0000	0.0000	0.0000	
MDF Base	0.2037	0.2723	-0.1080	0.0253	0.0006	0.0207	0.0214	0.0000	0.0000	0.0000	
Raspberry Pi 4*	0.0499	0.1782	-0.1090	0.0195	0.0003	0.0006	0.0009	0.0000	0.0000	0.0000	
Pixhawk Assembly*	0.0371	0.1815	-0.1112	-0.0098	0.0002	0.0006	0.0008	0.0000	0.0000	0.0000	
PDB Assembly*	0.0110	0.0869	-0.1080	0.0125	0.0001	0.0001	0.0002	0.0000	0.0000	0.0000	
Rear End Cap	0.1590	0.0030	-0.1080	0.0000	0.0017	0.0008	0.0009	0.0000	0.0000	0.0000	
Penetrator Bolt-Nut Assembly 1	0.0151	0.0029	-0.0934	-0.0275	0.0000	0.0001	0.0001	0.0000	0.0000	0.0000	
Penetrator Bolt-Nut Assembly 2	0.0151	0.0029	-0.0788	-0.0110	0.0000	0.0001	0.0001	0.0000	0.0000	0.0000	
Penetrator Bolt-Nut Assembly 3	0.0151	0.0029	-0.0788	0.0110	0.0000	0.0001	0.0001	0.0000	0.0000	0.0000	
Penetrator Bolt-Nut Assembly 4	0.0151	0.0029	-0.0934	0.0275	0.0000	0.0001	0.0001	0.0000	0.0000	0.0000	
Penetrator Bolt-Nut Assembly 5	0.0151	0.0029	-0.1225	0.0275	0.0000	0.0001	0.0001	0.0000	0.0000	0.0000	
Penetrator Bolt-Nut Assembly 6	0.0151	0.0029	-0.1371	0.0110	0.0000	0.0001	0.0001	0.0000	0.0000	0.0000	
Penetrator Bolt-Nut Assembly 7	0.0151	0.0029	-0.1371	-0.0110	0.0000	0.0001	0.0001	0.0000	0.0000	0.0000	
Penetrator Bolt-Nut Assembly 8	0.0151	0.0029	-0.1225	-0.0275	0.0000	0.0001	0.0001	0.0000	0.0000	0.0000	
Penetrator Bolt-Nut Assembly 9	0.0151	0.0029	-0.1080	-0.0110	0.0000	0.0001	0.0001	0.0000	0.0000	0.0000	
Penetrator Bolt-Nut Assembly 10	0.0151	0.0029	-0.1080	0.0110	0.0000	0.0001	0.0001	0.0000	0.0000	0.0000	
Bottom Ballast Weight 1*	0.1843	0.2168	-0.1080	0.0347	0.0002	0.0001	0.0003	0.0000	0.0000	0.0000	
Bottom Ballast Weight 2*	0.1843	0.2549	-0.1080	0.0347	0.0002	0.0001	0.0003	0.0000	0.0000	0.0000	
Bottom Ballast Weight 3*	0.1843	0.3359	-0.1080	0.0347	0.0002	0.0001	0.0003	0.0000	0.0000	0.0000	
Large Weight Camera Left*	0.1843	0.4732	-0.1454	0.0034	0.0001	0.0003	0.0002	0.0000	0.0000	0.0000	
Large Weight Camera Right*	0.1843	0.4732	-0.0705	0.0034	0.0001	0.0003	0.0002	0.0000	0.0000	0.0000	
Small Weight*	0.0283	0.1264	-0.0813	0.0193	0.0001	0.0000	0.0001	0.0000	0.0000	0.0000	
Right Tube											
Right Battery*	0.5650	0.3242	0.1205	-0.0114	0.0004	0.0028	0.0025	0.0000	0.0000	0.0000	
Left Battery*	0.5650	0.3242	0.0955	-0.0114	0.0004	0.0028	0.0025	0.0000	0.0000	0.0000	
Polycarbonate Tube*	2.0412	0.2660	0.1080	0.0000	0.0029	0.0230	0.0230	0.0000	0.0000	0.0000	
Front End Cap	0.1590	0.4752	0.1080	0.0000	0.0017	0.0008	0.0009	0.0000	0.0000	0.0000	
Front Flange Seal	0.1440	0.5150	0.1080	0.0000	0.0024	0.0013	0.0013	0.0000	0.0000	0.0000	
Rear Flange Seal	0.1440	0.0170	0.1080	0.0000	0.0024	0.0013	0.0013	0.0000	0.0000	0.0000	
MDF Base	0.2038	0.2721	0.1079	0.0253	0.0006	0.0207	0.0213	0.0000	0.0000	0.0000	
OLED Assembly*	0.0220	0.4587	0.1080	0.0260	0.0006	0.0003	0.0009	0.0000	0.0000	0.0000	
Jetson Orbitty Carrier Board*	0.0410	0.1747	0.1191	0.0023	0.0002	0.0006	0.0008	0.0000	0.0000	0.0000	
Jetson TX2*	0.0850	0.1747	0.1191	-0.0073	0.0002	0.0006	0.0008	0.0000	0.0000	0.0000	
Jetson Fan*	0.0590	0.1747	0.1191	-0.0223	0.0002	0.0007	0.0008	0.0000	0.0000	0.0000	
PDB Assembly*	0.0110	0.0869	0.1080	0.0125	0.0001	0.0001	0.0002	0.0000	0.0000	0.0000	
Rear End Cap	0.1590	0.0030	0.1080	0.0000	0.0017	0.0008	0.0009	0.0000	0.0000	0.0000	
Penetrator Bolt-Nut Assembly 1	0.0151	0.0029	0.1225	-0.0275	0.0000	0.0001	0.0001	0.0000	0.0000	0.0000	
Penetrator Bolt-Nut Assembly 2	0.0151	0.0029	0.1371	-0.0110	0.0000	0.0001	0.0001	0.0000	0.0000	0.0000	
Penetrator Bolt-Nut Assembly 3	0.0151	0.0029	0.1371	0.0110	0.0000	0.0001	0.0001	0.0000	0.0000	0.0000	
Penetrator Bolt-Nut Assembly 4	0.0151	0.0029	0.1225	0.0275	0.0000	0.0001	0.0001	0.0000	0.0000	0.0000	
Penetrator Bolt-Nut Assembly 5	0.0151	0.0029	0.0934	0.0275	0.0000	0.0001	0.0001	0.0000	0.0000	0.0000	
Penetrator Bolt-Nut Assembly 6	0.0151	0.0029	0.0788	0.0110	0.0000	0.0001	0.0001	0.0000	0.0000	0.0000	
Penetrator Bolt-Nut Assembly 7	0.0151	0.0029	0.0788	-0.0110	0.0000	0.0001	0.0001	0.0000	0.0000	0.0000	
Penetrator Bolt-Nut Assembly 8	0.0151	0.0029	0.0934	-0.0275	0.0000	0.0001	0.0001	0.0000	0.0000	0.0000	
Penetrator Bolt-Nut Assembly 9	0.0151	0.0029	0.1080	-0.0110	0.0000	0.0001	0.0001	0.0000	0.0000	0.0000	
Penetrator Bolt-Nut Assembly 10	0.0151	0.0029	0.1080	0.0110	0.0000	0.0001	0.0001	0.0000	0.0000	0.0000	
Bottom Ballast Weight 1*	0.1843	0.1930	0.1080	0.0347	0.0002	0.0001	0.0003	0.0000	0.0000	0.0000	
Bottom Ballast Weight 2*	0.1843	0.2676	0.1080	0.0347	0.0002	0.0001	0.0003	0.0000	0.0000	0.0000	
Bottom Ballast Weight 3*	0.1843	0.3136	0.1080	0.0347	0.0002	0.0001	0.0003	0.0000	0.0000	0.0000	
Large Weight Camera Left*	0.1843	0.4732	0.0705	0.0034	0.0001	0.0003	0.0002	0.0000	0.0000	0.0000	
Large Weight Camera Right*	0.1843	0.4732	0.1454	0.0034	0.0001	0.0003	0.0002	0.0000	0.0000	0.0000	

Externals										
Front Clamp Connector	0.0567	0.3278	0.0000	0.0000	0.0009	0.0003	0.0010	0.0000	0.0000	0.0000
Rear Clamp Connector	0.0567	0.0398	0.0000	0.0000	0.0009	0.0003	0.0010	0.0000	0.0000	0.0000
Back Thruster Support	0.1417	-0.0808	0.0000	0.0006	0.0004	0.0035	0.0036	0.0000	0.0000	0.0000
Clamp Set Left Rear*	0.1680	0.0398	-0.1080	0.0000	0.0037	0.0019	0.0019	0.0000	0.0000	0.0000
Clamp Set Left Front*	0.1680	0.3278	-0.1080	0.0000	0.0037	0.0019	0.0019	0.0000	0.0000	0.0000
Clamp Set Right Rear*	0.1680	0.0398	0.1080	0.0000	0.0037	0.0019	0.0019	0.0000	0.0000	0.0000
Clamp Set Right Front*	0.1680	0.3278	0.1080	0.0000	0.0037	0.0019	0.0019	0.0000	0.0000	0.0000
Left Thruster*	0.2950	-0.1414	-0.1001	0.0006	0.0009	0.0008	0.0008	0.0000	0.0000	0.0000
Mid Thruster	0.2950	0.4063	0.0000	0.0006	0.0008	0.0008	0.0009	0.0000	0.0000	0.0000
Right Thruster	0.2950	-0.1414	0.1001	0.0006	0.0009	0.0008	0.0008	0.0000	0.0000	0.0000
Small Weight Left*	0.0283	0.3278	-0.1778	0.0000	0.0001	0.0001	0.0000	0.0000	0.0000	0.0000
Small Weight Right*	0.0283	0.3278	0.1778	0.0000	0.0001	0.0001	0.0000	0.0000	0.0000	0.0000
TOTAL	12.3201	0.2538	0.0010	0.0021	0.1909	1.2050	1.3465	0.0023	-0.0003	0.0059

Table 9: LoCO Component Matrix for mass and moment of inertia determination.

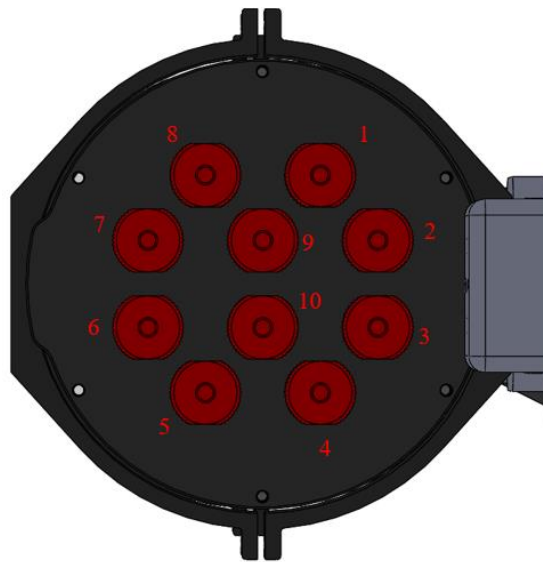


Figure 18: Clockwise penetrator numbering convention.